Numerical Investigation of Chemical Reactivity Effects on the Formation of Gaseous Oblique Detonation Waves

Chian Yan

A Thesis

in

The Department

of

Mechanical, Industrial and Aerospace Engineering

Presented in Partial Fulfillment of the Requirements

for the Degree of Master of Applied Science (Mechanical Engineering) at

Concordia University

Montreal, Quebec, Canada

July 2019

CONCORDIA UNIVERSITY
School of Graduate Studies

This is to certify that the thesis prepared

By: Chian Yan

Entitled: Numerical Investigation of Chemical Reactivity Effects on the Formation of Gaseous Oblique Detonation Waves

and submitted in partial fulfillment of the requirements for the degree of

Master of Applied Science (Mechanical Engineering)

complies with the regulations of the University and meets the accepted standards with respect to originality and quality.

Signed by the final examining committee

Dr. Carole El Ayoubi Chair

Dr. Fuzhan Nasiri Examiner

Dr. Charles Kiyanda Examiner

Dr. Hoi Dick Ng Thesis Supervisor(s)

Approved by _____
Chair of Department or Graduate Program Director

_____
Dean of Engineering and Computer Science

Date July 23, 2019

Abstract

Numerical Investigation of Chemical Reactivity Effects on the Formation of Gaseous Oblique Detonation Waves

Chian Yan

The concept of using oblique detonation waves for high efficiency propulsion systems have recently generated great interest in the development of air-breathing hypersonic aircraft due to their potential increased thermal efficiency through detonative combustion. However, for the proper design of an Oblique Detonation Wave Engine (ODWE), it is critical to predict the necessary conditions and understand the formation mechanism of oblique detonation waves. In this study, numerical simulations using a Graphics Processing Unit (GPU)-based solver are performed to investigate oblique detonations induced by a two-dimensional, semi-infinite wedge using the reactive Euler equations coupled with one-step Arrhenius or two-step induction-reaction kinetics. The novelty of this work lies in the analysis of chemical reaction sensitivity on the two types of oblique detonation formation, namely, the abrupt onset with a multi-wave point and a smooth transition with a curved shock. Scenarios with various inflow Mach number regimes M_0 and wedge angles θ are considered. The conditions for these two formation types are described quantitatively by the obtained boundary curves in M_0–E_a and M_0–k_R spaces. At a low M_0, the critical conditions for the transition are independent of the wedge angle. At a high flow Mach number regime with M_0 above approximately 9.0, the boundary curves for the three wedge angles deviate substantially from each other. The overdrive effect induced by the wedge becomes the dominant factor on the transition type. For large E_a the flow in the vicinity of the initiation region and subsequent ODW surface also exhibit more complex features.

Acknowledgements

First of all, my appreciation to my supervisor Dr. Hoi Dick Ng for his guidance during my graduate program. He is the guider who led me into this research field, inspired me in learning, gave me instructions during my research, and provided me with advice on this thesis. Secondly, I would like to show my deepest gratitude for my parents, for their constant support from over 10,000 kilometers away. Without their backup, I shall never have a chance to insist on my study. And I will thank all my colleagues who gave me valuable help and became friends with me, so that I do not feel lonely even if I am alone.

Table of Contents

List of Figures

List of Tables

Glossary

$\boldsymbol{\rho}$	Density
$\boldsymbol{t}$	Time
$\boldsymbol{e}$	Total energy
$\boldsymbol{\gamma}$	Ratio of specific heats, $\gamma = C_p/C_v$
$\boldsymbol{p}$	Pressure
$\boldsymbol{Q}$	Heat release
$\boldsymbol{\lambda}$	Reaction process variable (of single step Arrhenius model)
$\boldsymbol{\xi}$	Reaction progress variable (of two step induction-reaction model)
$\boldsymbol{T}$	Temperature
$\boldsymbol{R}$	Universal gas constant
$\boldsymbol{u}$	Fluid velocity on *x*-axis
$\boldsymbol{v}$	Fluid velocity on *y*-axis
$\boldsymbol{w}$	Fluid velocity on *z*-axis
$\dot{\boldsymbol{\omega}}$	Arrhenius reaction rate
$\boldsymbol{E_a}$	Arrhenius activation energy
$\boldsymbol{l_{1/2}}$	Half-reaction length
$\boldsymbol{k}$	Pre-exponential factor
$\boldsymbol{\Delta_I}$	Induction length
U	Conserved Variables
F	Flux
$\boldsymbol{k_R}$	Rate constant for the heat release
$\boldsymbol{u_{vn}}$	Post-shock particle velocity
$\boldsymbol{T_s}$	Post-shock temperature
$\boldsymbol{M_{cj}}$	Mach number of Chapman-Jouguet detonation
$\boldsymbol{\varepsilon}$	Normalized activation energy
V	Volume
$\boldsymbol{S}$	Wave speed
$\boldsymbol{\Delta x}$	Cell length in the mesh

$\boldsymbol{r}$	Ratio of slopes
$\mathbf{C}_{\boldsymbol{CFL}}$	CFL coefficient
$\boldsymbol{\theta}$	Wedge angle
$\boldsymbol{M_0}$	Initial Mach number
$\Delta_{\boldsymbol{i}}$	Slope vector
$\boldsymbol{\phi}$	Slope limiter
$\boldsymbol{f}$	Overdriven degree
$\boldsymbol{\beta}$	Oblique detonation angle
$\boldsymbol{D_{cj}}$	Chapman-Jouguet detonation velocity
$\boldsymbol{D}$	Overdriven detonation velocity

Chapter 1 Introduction

1.1 Fundamentals of detonations

The detonation phenomenon is the violent mode of combustion. It is a combustion-driven compression wave propagating at supersonic speed. Across a detonation, the pressure increases significantly; the temperature rise due to the adiabatic compression initiates the chemical reaction and the energy release and the expansion of the combustion products makes the detonation to be self-sustained. Detonations can occur in the form of solid, liquid and gases; the velocity propagating through the first two kinds of media are considerably much higher than the last one (Fickett & Davis 1979).

The detonation wave was formally observed and measured by Berthelot & Vieille and distinguished this distinct combustion mode by Mallard and Le Châtelier in the 1880s. The mathematical theory of detonation was first developed respectively by Chapman (1899) and by Jouguet (1905), which is now known as the Chapman-Jouguet (CJ) detonation. Their analysis is based on a control volume approach with thermodynamic equilibrium. To seek a unique solution of the conservation laws to determine both the detonation velocity and the states behind it, the Chapman-Jouguet condition requires that the particle velocity in shock-fixed frame reaches sonic velocity when the chemical reaction ends, i.e., fully burned products leaving the control volume enclosing the detonation wave. In a *p*-*v* diagram, this condition represents the tangency point between the Rayleigh line and the combustion product Hugoniot as shown in **Figure 1.1**. It is shown that the prediction by CJ detonation condition usually provides a result within 2% error compared with experimental results.

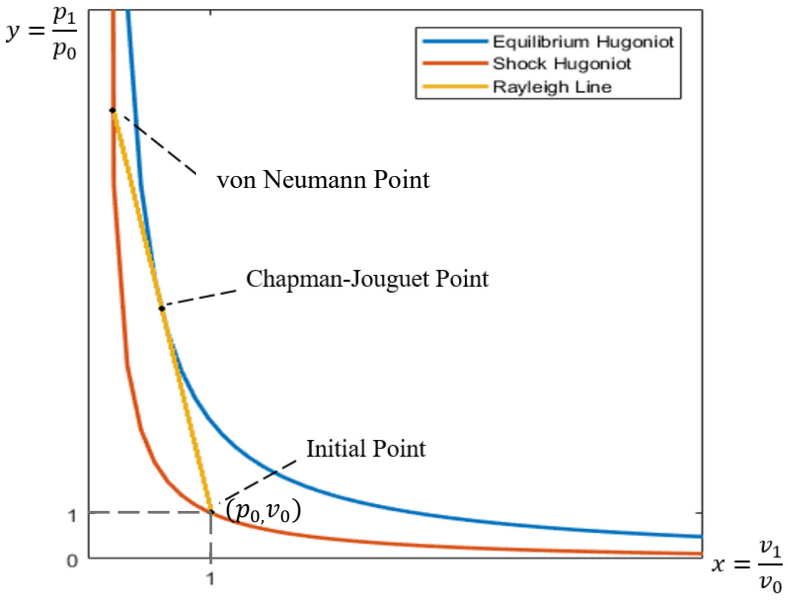

Figure 1.1 *p-v* diagram and the Chapman-Jouguet condition.

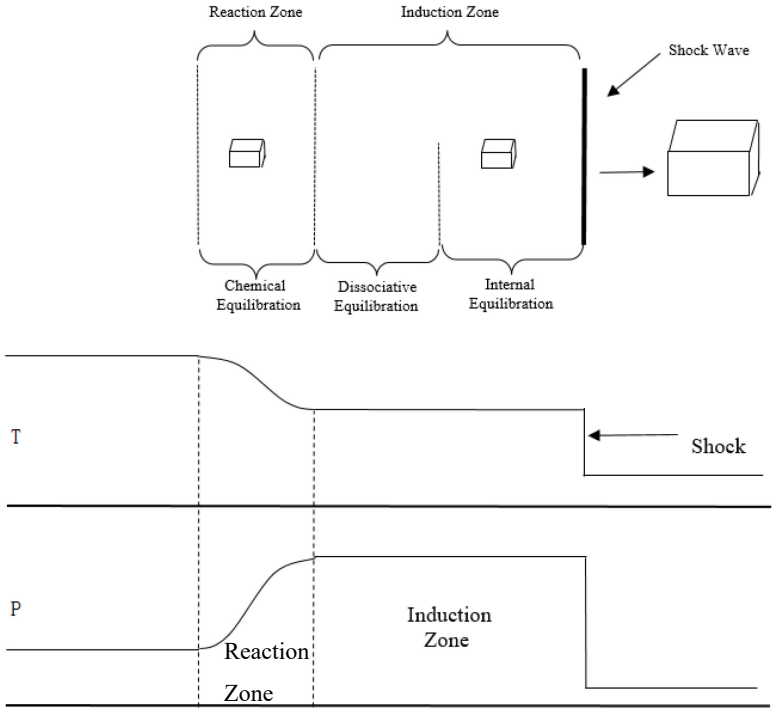

Figure 1.2 ZND description of the detonation structure.

The steady structure of a detonation wave was described in the 1940s independently by Zel'dovich (1940), von Neumann (1942), and Döring (1943), which

has come to be known as the ZND model, see **Figure 1.2**. The classic ZND model describes the detonation as a structure consisted of an inert normal shock followed by a chemical reaction zone. The post-shock condition (or von Neumann state) triggers the chemical reaction and after a thermally neutral induction zone, the exothermic chemical reaction proceeds. The flow within the reaction zone is subsonic. At the end of the reaction zone, the flow reaches locally sonic in accordance to the Chapman-Jouguet condition. The importance of the ZND model is that it provides the basic propagation mechanism, i.e., the detonation is sustained by the chemical energy release caused by auto-ignition via adiabatic shock compression and the work done by the expansion behind the shock front.

However, the ideal ZND model postulates that the detonation wave is of steady one-dimensional configuration and the structure predicted by this one-dimensional theory is seldom observed. The non-linear, intrinsic oscillatory behavior of one-dimensional detonations with simple chemistry has also been shown numerically by Fickett & Wood (1966) using the method of characteristics. Since then, more thorough studies on one-dimensional pulsating detonations have been carried out by numerous researchers, e.g., Bourlioux *et al.* 1991, 1992; He & Lee 1995; Sharpe & Falle 2000; etc. Theoretical hydrodynamic stability analyses have shown that the steady ZND structure is inherently unstable to small perturbations (Erpenbeck 1962, 1964; Lee & Stewart 1990; Sharpe 1997; Short & Stewart 1998). Both direct numerical simulations (Taki & Fujiwara 1978; Oran *et al.* 1982, 1988; Lefebvre & Oran, 1995; Fujiwara & Reddy, 1989; Bourlioux & Majda, 1992; Tsuboi *et al.* 2002; Williams *et al.* 1997; Kailasanath *et al.* 1985; Sharpe 2001) and experimental visualization results (White 1961; Strehlow *et al.* 1967; Oppenheim 1985; Austin *et al.* 2005) revealed that gaseous detonations were always unstable and three-dimensional. The unsteady detonation structure consists of an ensemble of interacting transverse shock waves sweeping back and forth across the leading front, see **Figure 1.3**. Similar to the classical supersonic flows (Courant & Friedrichs 1948), the mutual interactions of these shocks form the classical triple shock Mach interaction configuration. The trajectories of these triple

points can be recorded on a smooth surface coated with a carbon soot deposit and have a characteristic fish scale or cellular pattern as the detonation propagates by it as shown in **Figure 1.4**. These interactions give rise to what we refer to as cellular detonation instability – a manifestation of the instability of the front caused by the unsteady coupling between the chemical reactions and the gas dynamic flow field.

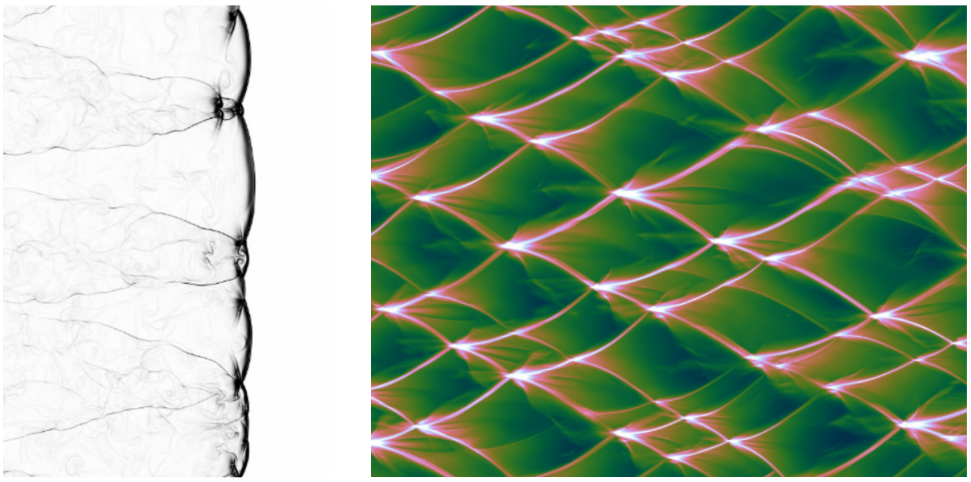

Figure 1.3 Numerical results showing the schlieren plot and soot foil of cellular detonation.

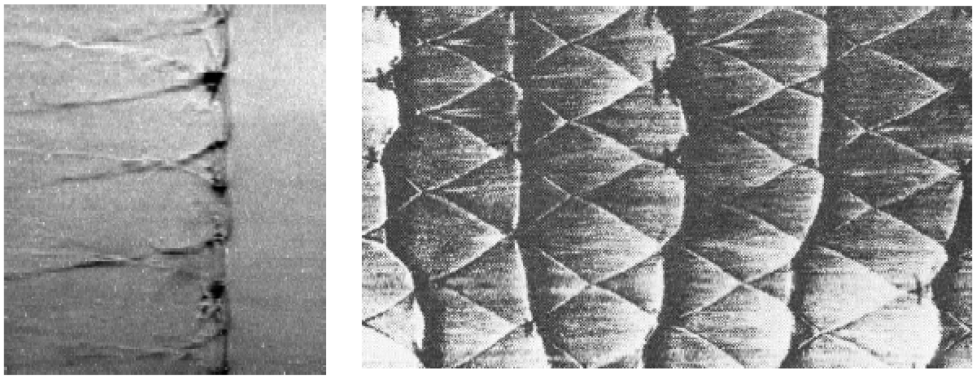

Figure 1.4 Schlieren photograph and smoked foil showing the cellular structure for $2H_2 + O_2 + 2Ar$ detonation (Radulescu 2003; Strehlow 1969).

In spite of the extensive efforts to study the behavior of detonations thus far, it remains un-resolved to fully understand the coupled chemical hydrodynamic interactions responsible for the self-sustained detonation formation and its dynamic cellular structure (Lee 2008). This stems mainly from the fact that the associated phenomena are highly complex and involve many aspects of combustion and gas dynamic processes. The initiation mechanism, the role of instability and the detailed

chemical kinetics processes within the reaction zone structure are the key ingredients and understand their influences are crucial so that the detonation structure can be correctly characterized.

Fundamental aspects and outstanding issues of detonations can be found in the comprehensive monograph by Lee (2008). Other comprehensive discussions on recent detonation modeling can be found in recent reviews (Shepherd 2009; Oran 2015).

1.2 Propulsion applications using detonative combustion

Traditionally, the detonation phenomenon is of main concern to many safety engineering applications and industrial processes in the chemical and energy sectors due to its pressure and temperature rise, causing damage and causalities. The detonation research primarily focuses on the ability to predict the detonation explosives, the initiation of detonation, and the limits that are critical to proper risk rate of chemical facilities, prevention of unexpected accidence and the transportation safety for hazardous materials (Ng & Lee 2008). In recent years, however, the focus has shifted to the use of the energy release by this supersonic, self-sustained, combustion-driven wave. The detonative combustion is progressively turning into a viable option for the development of advanced air-breathing hypersonic propulsion systems which harness the conditions generated by this combustion mode to achieve a high thermal cycle efficiency (Kailasanath 2003; Wolanski 2013). Examples include the concept of Pulse Detonation Engines (PDEs) and continuous detonation engines such as rotating detonation and oblique detonation engine devices. The latter is the focus of this thesis. These engines produce either short bursts or continuous thrusts and can be used for commercial, military and space flight purposes. Compared to jet engines, they have higher efficiency and can operate at hypersonic speeds. These PDEs also have simpler concepts of design which involve almost few moving parts; therefore, they have higher reliability and lower maintenance costs (Roy *et al.* 2004).

1.3 Oblique detonation wave (ODW)

Among different detonation-based propulsion concepts, oblique detonation wave (ODW) has been studied and given rise to the development of Oblique Detonation Wave Engines (ODWEs) (Wolanski 2013) and Ram Accelerators (Hertzberg *et al.* 1991; Higgins 2006). This class of propulsion systems not only keeps the advantages of the supersonic combustion ramjet (Scramjet), but also manages a high efficiency in thermal cycle through the detonation mode of combustion (Alexander *et al.* 2008; Chan *et al.* 2010). The oblique detonation propulsion concept has thus great potentials for applications in hypersonic conditions.

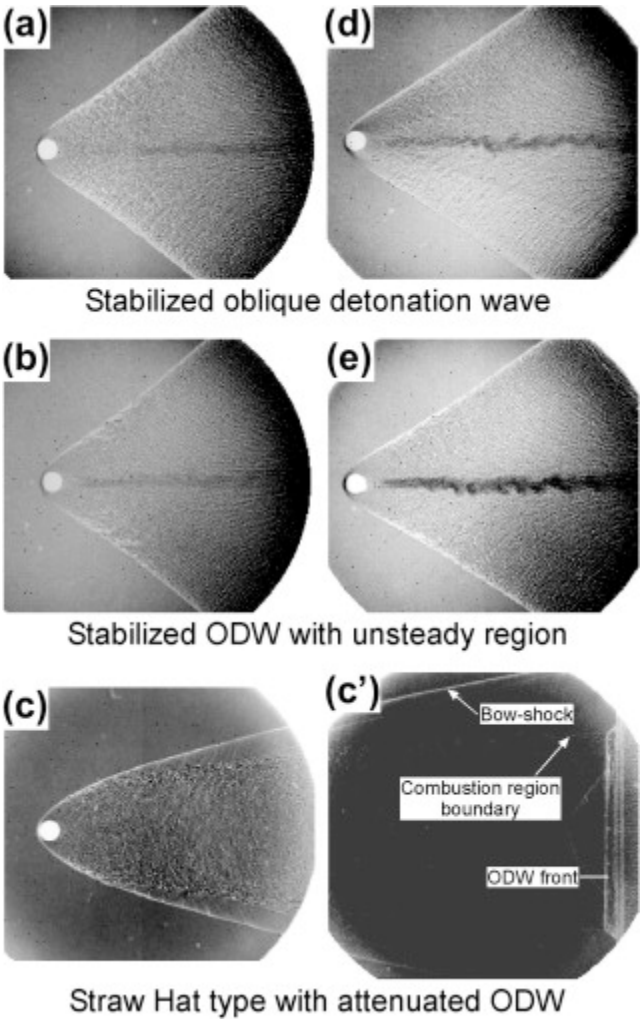

Figure 1.5 Oblique detonation initiation by a hypersonic projectile (Maeda *et al.* 2012).

In the 1960-70s, the oblique detonation wave has been researched in detail by launching a hypersonic blunt projectile into combustible mixtures (McVey & Toong 1971; Lehr 1972). These studies focus primarily on the conditions required to initiate an oblique detonation wave in the combustible mixture. Depending on the test conditions such as the projectile speed and mixture initial conditions, different combustion regimes were observed around the blunt body, e.g., a prompt or delayed ODW, combustion instabilities, a wave splitting, or an inert shock wave Criteria based on the energetic and chemical kinetic limits are proposed to predict the conditions and interpret the observed flow field regimes in terms of competing reactions and flow-quenching effects, e.g., Kaneshige & Shepherd (1996); Lee (1997); Ju *et al.* (1998a, b); Kasahara *et al.* (2001); Verreault & Higgins (2011); Maeda *et al.* (2012), see **Figure 1.5**.

However, for a more practical configuration for propulsion engine operation, an oblique detonation wave can be induced by a wedge in an incoming reactive flow (Adelman *et al.* 1988; Cambier *et al.* 1990; Viguier *et al.* 1996; Morris *et al.* 1998). A schematic of an ODW engine and the wedge-induced oblique detonation is shown in **Figure 1.6**. The supersonic inflow of the pre-mixed combustible gas induces the oblique detonation wave from the wedge. In general, an oblique shock wave (OSW) first forms when the flow interacts with the wedge, and that ignites the combustible reactants. In a short period of time, the oblique shock wave subsequently transits into an oblique detonation wave (ODW). Such standing oblique detonation wave configuration attached to the wedge tip presents a practical configuration for engine operation. For applications in propulsion systems, it is vital to determine whether the formation of the standing oblique detonation wave is robust and whether its structure can always be stabilized over a wedge at a desirable location. Due to the strong coupling sensitivity between fluid dynamics and chemical reactions, as well as the inherent unstable nature of the detonation wave, in fact it remains technically challenging to establish the steady oblique detonations in high-speed combustible mixtures for practical propulsion applications, and such success requires fundamental understanding

of the oblique detonation structure and its unsteady formation process.

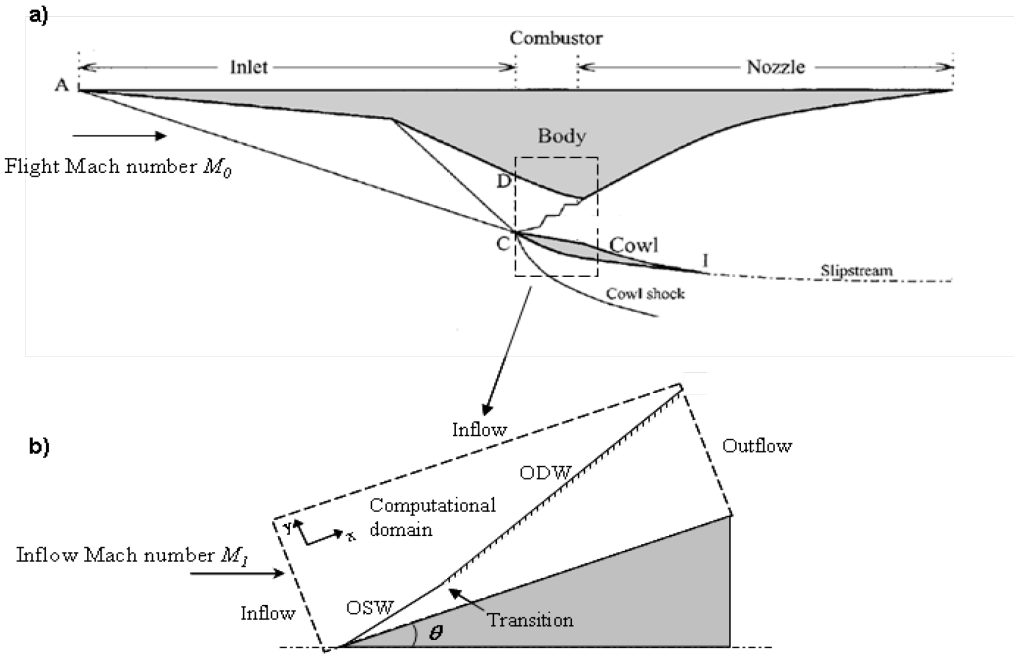

Figure 1.6 a) Sketch of an oblique detonation engine; and b) the ODW induced by a wedge.

In the literature a wealth of research studies on oblique detonations can be found. There has been indeed a remarkable progress in understanding the fundamental aspects of oblique detonation waves induced by a semi-infinite, two-dimensional wedge. For instance, analytical solutions such as wave angles and steady structures as the basic foundation were sought in a number of pioneering works using detonation polar analysis by approximating the ODW as an oblique shock wave (OSW) coupled with an instantaneous post-shock heat release (Gross 1963; Pratt *et al.* 1991; Ashford & Emanuel 1994; Emanuel & Tuckness 2004). In later studies, using numerical simulation Li *et al.* (1994) revealed that the multi-dimensional oblique detonation structure consists of a non-reactive oblique shock, an induction region, a set of deflagration waves, and an oblique detonation surface, all united on a multi-wave point giving rise to a λ-like formation ODW structure as shown in **Figure 1.7**. Such classical structure was verified from experiments, and is often considered as the standard model of oblique detonations. As the propagation of all multi-dimensional, gaseous detonation waves is inherently unstable (Lee 2008; Ng & Zhang 2012), the formation of cellular structure

and fine scale instability on the established oblique detonation surface are also revealed numerically downstream of the kink-like oblique shock-to-detonation transition (Choi *et al.* 2007; Gui *et al.* 2011, 2012). Nevertheless, later studies had revealed that there exists other type of transition structures due to various complicated unsteady processes. Particularly, Vlasenko & Sabelnikov (1995) and Da Silva *et al.* (2000) showed that the shock-to-detonation transition may occur smoothly by a curved shock, rather than occurring in a multi-wave interaction point, also see **Figure 1.7**.

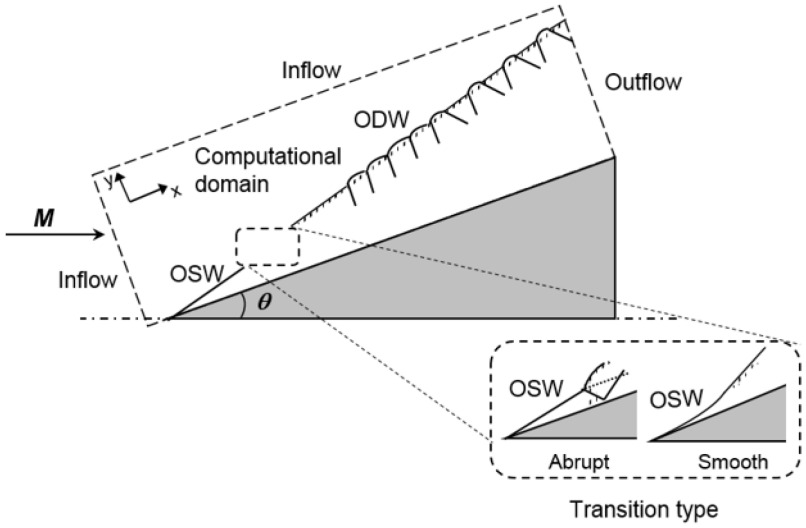

Figure 1.7 A schematic of the computational details and ODW phenomena.

With the advance in scientific computing using parallel Central Processing Units (CPUs) and Graphics Processing Units (GPUs) computing technology (Vanka 2013; Betelin *et al.* 2017), there has been significant advance in investigating in detail the unsteady oblique detonation formation and its structure. Using high-resolution numerical simulations, various peculiar formation structures of wedge-induced oblique detonation waves, i.e., the transition from the oblique shock wave (OSW) to the oblique detonation wave (ODW), have been revealed in recent investigations e.g., (Papalexandris 2000; Teng & Jiang 2012; Liu *et al.* 2016; Wang *et al.* 2015). Hysteresis phenomenon of the ODW structure related to initial condition and ODW responses subject to inflow non-uniformities and turbulences have also been investigated (e.g., Iwata *et al.* 2017; Zhang *et al.* 2018).

Among all the ODW studies, the two aforementioned fundamental formation structure, namely, the abrupt transition from OSW to ODW where a nonreactive oblique shock, a set of deflagration waves, and the oblique detonation surface, all united on a multi-wave point; and the smooth transition characterized by a smoothly curved shock have been carefully performed using numerical simulations (Vlasenko & Sabelnikov 1995; Papalexandris 2000; Da Silva *et al.* 2000; Teng & Jiang 2012). These numerical simulations indicate that the type of transition processes depends on both chemical and aerodynamic parameters. Although it is qualitatively found that the smooth transition usually appears in the cases with a high Mach number and weak chemical sensitivity with a low activation energy of the reactive mixture, the quantitative conditions are yet to be fully determined.

1.4 Objective of the thesis

In this work, a parametric numerical study is presented to address the effect of chemical reaction sensitivity and length scales on the ODW initiation structure. Following previous studies, the ODW phenomena are simulated using an ideal-gas, reactive flow model given by the inviscid Euler equations with one-step irreversible Arrhenius or two-step induction-reaction kinetics (Ng *et al.* 2005; Yang *et al.* 2018; Tang-Yuk *et al.* 2018). Although numerical simulations using complex chemistry with detailed chemical reaction rates are nowadays possible with increasing computational resources, it remains challenging to fully interpret the tremendous amount of chemical kinetic and flow field information that is generated from the computation. Hence, for a fundamental contribution, this idealized model is shown to provide key results elucidating the underlying physics of the ODW dynamics. In addition, the two-step induction-reaction kinetics, consisting of a thermally neutral induction step followed by a main heat release reaction layer, provides a compromise on the detailed chemistry model. It retains the simplicity of global kinetics but is detailed enough to mimic salient

features of real combustion governed by chain-branching kinetics, allowing the introduction of two length scales, i.e., induction and reaction lengths, apart from the temperature sensitivities governed by the activation energy (Ng *et al.* 2005). In this parametric study, computations were carried out over a wide range of activation energy E_a (non-dimensionalized with respect to the initial pre-shock state) from 20 to 60 using the one-step Arrhenius kinetics, heat release rate constant k_R from 1 to 10 for the two-step kinetics, three wedge angles θ and different inflow Mach number M_0. It is worth noting that the high E_a regime considered in this work has not been explored thoroughly in any previous studies due to the numerical resolution requirement. Boundaries separating the two aforementioned transition types are obtained and new features resulting from the effect of high activation energy on the flow structure in the vicinity of the ODW initiation region and the fully developed ODW unstable surface are discussed in detail.

1.5 Thesis outline

Current chapter of this thesis is an introduction for some basic concepts and background information of the related literature. Also in this chapter, a preamble of the methodology applied in this research and the objective are given. Chapter 2 gives the detailed description of the physical model and numerical method used in the computation. Chapter 3 presents the results of numerical simulations and analyses of the outcomes. The final Chapter 4 concludes this investigation and provides suggestions for future works.

1.6 Contribution to knowledge

This investigation contributes, using numerical simulations, to the understanding of the effect of chemical reaction kinetics on the formation process of oblique detonation waves induced by a semi-infinite, two-dimensional wedge. The results

identify quantitatively the kinetic conditions distinguishing two OSW-ODW transition process, namely the abrupt and smooth transition as shown in **Figure 1.7**.

This thesis includes published works in Aerospace – An open Access Journal of aeronautics and astronautics published by MDPI with the following reference:

- Yan, C., Teng, H., Mi, X.C. and Ng, H.D. The effect of chemical reactivity on the formation of gaseous oblique detonation waves. *Aerospace (MDPI)*, **2019**, 6(6), 62. [https://doi.org/10.3390/aerospace6060062]

Chapter 2 Formulations and Numerical Methods

Throughout this thesis, numerical simulation is used as the research methodology. It is of great importance to formulate the relevant physical model and evaluate the numerical technique applied in current simulation of the compressible reactive flow. Hence, in this chapter, governing equations are introduced and numerical methods consisting of the HLLC approximate Riemann solver with MUSCL-Hancock reconstruction for approximating solutions of those equations are discussed. The numerical solver is implemented using NVIDIA CUDA framework and run on Graphical Processing Unit (GPU) hardware Tesla K40 to achieve high computing performance and acceleration.

2.1 Governing equations

For the numerical simulation performed in this thesis, an ideal model based on Euler equations is chosen to describe the gas flow in the system. In reality, the model should be viscousk, which brings viscosity, to capture shock thickness and other dissipative effects. However, due to all the conditions we investigate are at relatively high Reynolds number, thus we can indeed consider the viscous effects negligible. For the high Mach number flow, diffusion effects are also neglected due to the time scale of the phenomenon involved. In fact, the viscous and diffusive effects are shown to have insignificant influence on the overall ODW structure by Li *et al.* (1993). To mimic chemical reaction of the combustible mixture, both a one-step global reaction with an Arrhenius rate law and a two-step induction-reaction model are used.

Neglecting the viscous and diffusive effects, the governing equations for the ODW flow dynamics are thus simplified into the reactive Euler equations as follows:

$$\frac{\partial \mathbf{U}}{\partial t} + \frac{\partial \mathbf{F}(\mathbf{U})}{\partial x} + \frac{\partial \mathbf{G}(\mathbf{U})}{\partial y} = \mathbf{S}(\mathbf{U})$$

$$\mathbf{U} = \begin{pmatrix} \rho \\ \rho u \\ \rho v \\ \rho e \\ \rho \lambda \end{pmatrix}, \quad \mathbf{F}(\mathbf{U}) = \begin{pmatrix} \rho u \\ \rho u^2 + p \\ \rho uv \\ (\rho e + p)u \\ \rho u \lambda \end{pmatrix}, \quad \mathbf{G}(\mathbf{U}) = \begin{pmatrix} \rho v \\ \rho uv \\ \rho v^2 + p \\ (\rho e + p)v \\ \rho v \lambda \end{pmatrix}, \quad \mathbf{S}(\mathbf{U}) = \begin{pmatrix} 0 \\ 0 \\ 0 \\ 0 \\ \rho \dot{\omega} \end{pmatrix}$$

where the **U** is the conserved variable, **F** and **G** are the convective fluxes and **S** is reactive source term. For the polytropic equation of state e is the total energy per unit mass given by:

$$e = \frac{p}{(\gamma-1)\rho} + \frac{(u^2+v^2)}{2} + \lambda Q$$

With the ideal gas equation of state:

$$T = \frac{p}{\rho}$$

All the flow variables and chemical parameters have been made dimensionless by reference to the uniform unburned quiescent state ahead of the detonation front, i.e.:

$$\rho = \frac{\tilde{\rho}}{\rho_0}\ ,\ p = \frac{\tilde{p}}{p_0}\ ,\ T = \frac{\tilde{T}}{T_0}\ ,\ u = \frac{\tilde{u}}{\sqrt{RT_0}}\ ,\ x = \frac{\tilde{x}}{x_{ref}}\ ,\ Q = \frac{\tilde{Q}}{RT_0}\ ,\ E_a = \frac{\widetilde{E_a}}{RT_0}$$

The above governing equations are coupled with a chemical kinetic law for the reaction rate $\dot{\omega}$. In this study, two different reaction rate laws were considered, i.e., single-step kinetics and two-step induction-reaction kinetics. The single-step irreversible chemical reaction model with an Arrhenius rate law is given as:

$$\dot{\omega} = -k\lambda \exp(\frac{-E_a}{T})$$

in which the reaction sensitivity is governed by E_a. The pre-exponential constant for a given mixture k is used to define the spatial and temporal scales, so by solving the steady Zel'dovich-von Neumann-Döring (ZND), one-dimensional, Chapman-Jouguet (CJ) detonation, the half reaction zone length $l_{1/2}$ is unity (Bourlioux 1991; Ng & Zhang 2012; Higgins 2012). The variable λ is the mass fraction of the reactant, used to indicate the reaction progress. In this study, λ equals 1 when the chemical reaction has not get started and all the reactants stay unburnt, and 0 when all reactant has been totally consumed, which means the chemical reaction is completed. For an Arrhenius rate law,

$\dot{\omega}$ is only influenced by temperature. The parameter Q is the amount of heat release non-dimensionalized by RT_0.

A more realistic reaction model (Ng *et al.* 2005) includes an induction zone with an additional advection equation for ξ. The reaction zone is modeled in the same way and the induction zone is also of an Arrhenius type as follows:

$$\dot{\omega}_I = H(1-\xi)\cdot k_I \exp\left[E_I\left(\frac{1}{T_s}-\frac{1}{T}\right)\right]$$

$$\dot{\omega}_R = -(1-H(1-\xi))\cdot \lambda k_R \exp\left(\frac{-E_R}{T}\right)$$

where ξ is the progress variable in the induction process and $H(1-\xi)$ a step function, i.e.:

$$H(1-\xi)\begin{cases} = 1 & \text{if } \xi < 1 \\ = 0 & \text{if } \xi \geq 1 \end{cases}$$

In the two-step kinetic model, the reference length scale x_{ref} is chosen such that the one-dimensional ZND induction length Δ_I is unity, i.e., $k_I = -u_{vn}$ where u_{vn} is the particle velocity behind the shock front in the shock-fixed frame for the Chapman-Jouguet (CJ) detonation. T_s is the temperature at the shocked state of the ZND detonation. From the Rankine-Hugoniot relationships (Ng & Zhang 2012), the Mach number of Chapman-Jouguet detonation (CJ detonation) can be found as:

$$M_{CJ} = \frac{D}{c_0} = \sqrt{\left(1+\frac{\gamma^2-1}{\gamma}Q\right)+\sqrt{(1+\frac{\gamma^2-1}{\gamma}Q)^2-1}}$$

With the Mach number of CJ detonation, we can find:

$$u_{vn} = \sqrt{\gamma}\cdot\frac{2+(\gamma-1)M_{CJ}^2}{(\gamma+1)M_{CJ}}$$

In addition the post-shock temperature of the ZND detonation can be obtained by:

$$T_s = \frac{[2\gamma M_{CJ}^2-(\gamma-1)][2+(\gamma-1)M_{CJ}^2]}{(\gamma+1)^2 M_{CJ}^2}$$

In detail, the induction index ξ is introduced as a reaction progress variable for the ignition period and $H(1-\xi)$ equals 1 if $\xi < 1$ or $H(1-\xi)$ equals 0 if $\xi \geq 1$ indicating the end of the induction zone, $x = 1$. After this point, the second step for the heat release begins and similar to the one-step model, λ is the reaction process variable and k_R is the

rate constant for the heat release. Again, the local chemical energy that has been released at any instant during the reaction is equal to λQ. The pre-exponential factor k_R is used in this work to vary the reaction zone structure (Ng *et al.* 2005).

There are two associated activation energies, namely E_I and E_R, which are rescaled for convenient by the temperature jump across the leading shock of the detonation, i.e.:

$$E_I = \varepsilon_I T_s,\ E_R = \varepsilon_R T_s$$

where T_s is the post-shock temperature jumping across the leading front shock. For normal hydrocarbon mixed reactants, the activation energy of the induction stage ε_I should be relatively large because in the induction zone, high energy level is required to break the strong chemical bonds of the reactants and transfer them into radicals. Typical values for ε_I usually ranges from 4 (for H_2/O_2 mixture) to 12 (for heavy hydrocarbon mixtures). However, the second step involves only reactions between free radicals which have already been stimulated. For typical chain-branching reactions, therefore, the first step reaction in the induction stage generally has a larger activation energy compared to the second step. So for present study, we have:

$$E_I \gg E_R \qquad \varepsilon_I \gg \varepsilon_R$$

2.2 Numerical methods

To solve the equations of the conservation laws governing the dynamics of reactive flow, reliable numerical methods should be found. Some extra source terms for detonation progress, chemical reaction kinetics and the propagation of flows should be taken into account.

2.2.1 Operator splitting

For a system of equations in two dimensions with the reactive source term, i.e.,

$$\frac{\partial \mathbf{U}}{\partial t} + \frac{\partial \mathbf{F}(\mathbf{U})}{\partial x} + \frac{\partial \mathbf{G}(\mathbf{U})}{\partial y} = \mathbf{S}(\mathbf{U})$$

F and **G** are the convection fluxes of *x*- and *y*-direction, respectively, and **S** is the reaction source term. If the entire operators are being solved at the same time in a single

time-step Δt, the process will be technically involved using un-splitted numerical techniques. Alternatively, in an operator splitting scheme the time-step Δt is assumed to be sufficiently small, thus allowing each operator to be applied independently of the others, i.e., for the numerical integration to treat separately the hydrodynamics process in each direction (convective terms associated with $\mathbf{F}(\mathbf{U})$ and , $\mathbf{G}(\mathbf{U})$) and the chemical reaction process (reactive term $\mathbf{S}(\mathbf{U})$). Denoting $\mathcal{L}_x$, $\mathcal{L}_y$ and $\mathcal{L}_S$ to be the operators for the convective terms in each direction and for the source term, respectively, the operating scheme thus follows:

$$\frac{\partial \boldsymbol{U}}{\partial t} + \mathcal{L}_x \boldsymbol{U} = 0, \qquad \boldsymbol{U}^n \rightarrow \boldsymbol{U}^{n+\frac{1}{3}}$$
$$\frac{\partial \boldsymbol{U}}{\partial t} + \mathcal{L}_y \boldsymbol{U} = 0, \quad \boldsymbol{U}^{n+\frac{1}{3}} \rightarrow \boldsymbol{U}^{n+\frac{2}{3}}$$
$$\frac{d\boldsymbol{U}}{dt} = \boldsymbol{S}(\boldsymbol{U}), \quad \boldsymbol{U}^{n+\frac{2}{3}} \rightarrow \boldsymbol{U}^{n+1}$$

First, $\mathcal{L}_x$ is solved by using an one-dimensional Riemann solver, followed by $\mathcal{L}_y$ and then the spatially homogeneous problem integrated numerically using conventional techniques for $\mathbf{S}(\mathbf{U})$. In operator form, it is given as:

$$\mathbf{U}_i^{n+1} = \mathcal{L}_S^{\Delta t/3} \mathcal{L}_y^{\Delta t/3} \mathcal{L}_x^{\Delta t/3} \mathbf{U}_i^n$$

2.2.2 Riemann problem and Godunov's method

The governing equations are constructed on a set of partial differential equations and we need to solve those PDEs by reliable numerical methods. To solve the Euler equations, a finite volume control system can first be introduced. For a one-dimensional (1-D) system of PDEs written in conservative form:

$$\mathbf{U}_t + \mathbf{F}(\mathbf{U})_x = 0$$

U is the conserved variables and **F** is the convective fluxes. Integrate the upper equation over a single cell length and we can get:

$$\int \mathbf{U} dx = -\int \mathbf{F}(\mathbf{U}) dt$$

The Riemann problem for the one-dimensional time-dependent Euler equations is with

the initial condition:

$$\mathbf{U}(t=0,x)=\begin{cases}\mathbf{U}_L & x\le 0\\ \mathbf{U}_R & x>0\end{cases}$$

As illustrated in **Figure 2.1**, with the initial conditions $\mathbf{U}_{\mathrm{i}}^{\mathrm{n}}$ and $\mathbf{U}_{\mathrm{i+1}}^{\mathrm{n}}$the Riemann problem can be solved at time $t=\Delta t$ to obtain the conserved variables at the cell interface $\mathbf{U}_{\mathrm{i+\frac{1}{2}}}^{\mathrm{n}}$, and with which $\mathbf{F}_{\mathrm{i+\frac{1}{2}}}$ can then be computed. Note that, in 1-D condition, at the surface of each cell, we can just focus on the left and right point and integrate the equation over time to give:

$$\mathbf{U}_i^{n+1}=\mathbf{U}_i^n-\frac{\Delta t}{\Delta x}\left[\mathbf{F}^n_{i+\frac{1}{2}}-\mathbf{F}^n_{i-\frac{1}{2}}\right].$$

So with this equation combined with the fluxes at each cell boundary $\mathbf{F}_{\mathrm{i+\frac{1}{2}}}$, the conserved variable for next time step can be computed.

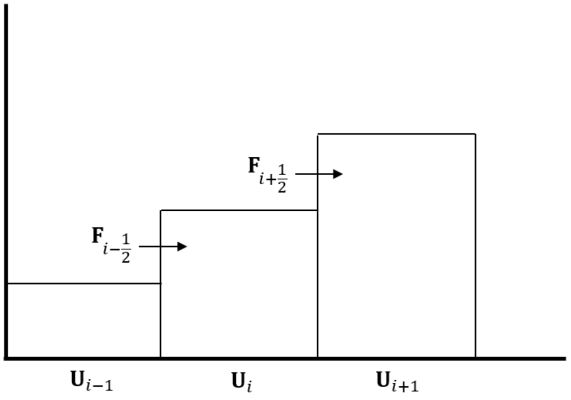

Figure 2.1 Intercell flux **F** computed at the boundaries of piecewise constant cells using the Riemann problem solutions.

In 1959, Godunov presented his flux:

$$\mathbf{F}_{i+\frac{1}{2}}=\mathbf{F}(\mathbf{U}_{i+\frac{1}{2}}(0))$$

where $\mathbf{U}_{i+\frac{1}{2}}(0)$ is the exact similarity solution $\mathbf{U}_{i+\frac{1}{2}}(x/t)$ of the Riemann problem, evaluated at *x/t* = 0. The structure of the Riemann problem consists of left-going and right-going shock or rarefaction waves in various allowed combinations, separated by a contact surface.

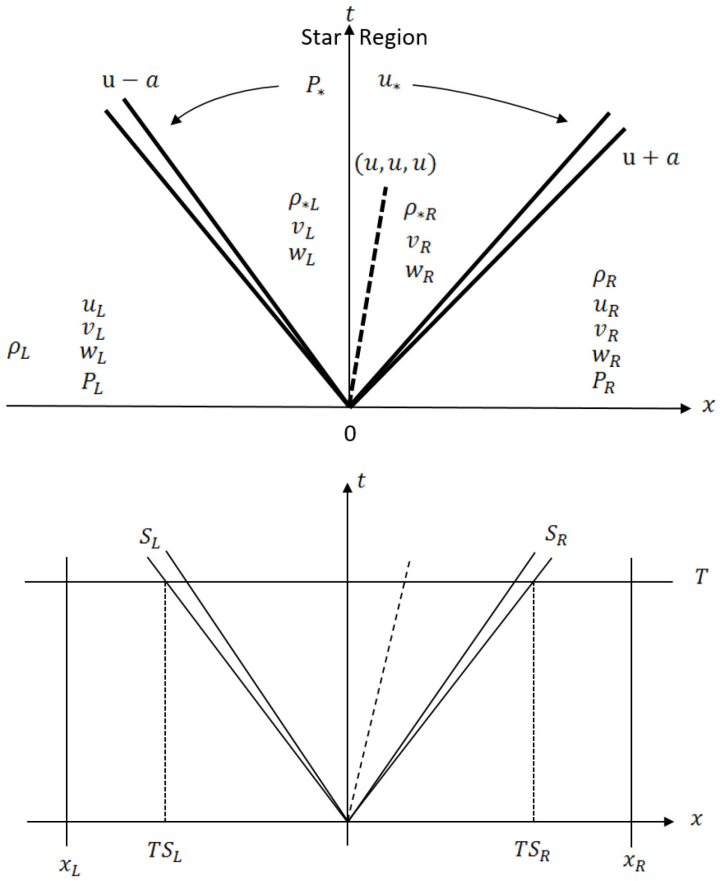

Figure 2.2 Waves structure of the exact solution $\mathbf{U}_{i+\frac{1}{2}}(x/t)$ of the Riemann Problem for the one-dimensional Euler equations (upper) and control volume (lower)$[x_L, x_R] \times [0, T]$.

Consider **Figure 2.2** showing the whole structure arising from the exact solution of the Riemann problem in the control volume $[x_L, x_R] \times [0, T]$. The integral relation can be expressed as:

$$\int_{TS_L}^{TS_R} \mathbf{U}(x,T)dx = T(S_R\mathbf{U}_R - S_L\mathbf{U}_L + \mathbf{F}_L - \mathbf{F}_R)$$

where S_L and S_R are the fastest signal velocities and T is a chosen time. On division through by the length $T(S_R - S_L)$, which is the width of the wave system of the solution of the Riemann problem between the slowest and fastest signals at time T, we have:

$$\frac{1}{T(S_R - S_L)}\int_{TS_L}^{TS_R} \mathbf{U}(x,T)dx = \frac{S_R\mathbf{U}_R - S_L\mathbf{U}_L + \mathbf{F}_L - \mathbf{F}_R}{S_R - S_L}$$

2.2.3 HLLC approximate Riemann solver

For the purpose of directly computing numerical fluxes, approximate techniques have been developed for solving the Riemann problem approximately and the resulting algorithms have been known as Harten, Lax and van Leer (HLL) approximate Riemann solvers. Unlike the analytical approach to solve the exact Riemann problem giving a vast amount of information, which is time consuming, approximate Riemann solver gives an estimation for the intercell numerical flux directly, and the differences in result are generally negligible. The HLL Riemann solver assumes a single constant state between two nonlinear waves (shock or rarefaction) and requires estimates for the fastest signal velocities emerging from the initial discontinuity at the interface, resulting in a the two-wave model for the solution structure of the problem. The HLLC scheme used in this work is an extension of the HLL scheme wherein the missing contacts and shear waves are put back into the structure of the original approximate solver. The HLLC scheme provides a more accurate approach with a three-wave model, preserving the solution structure with shock, contact, and shear waves. To compute wave speeds of the left-going and right-going wavesS_L andS_R, the pressure-velocity based wave estimations presented by Toro (2006) are used to estimate the shock and the rarefaction waves accurately.

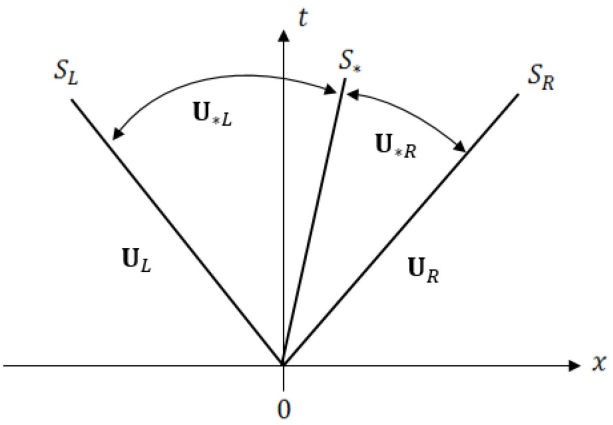

Figure 2.3 HLLC approximate Riemann solver. Solution in the Star Region consists of two constant states separated from each other by a middle wave of speed S_*.

From the integral relation derived previously:

$$\frac{1}{T(S_R - S_L)} \int_{TS_L}^{TS_R} \mathbf{U}(x,T)dx = \frac{S_R \mathbf{U}_R - S_L \mathbf{U}_L + \mathbf{F}_L - \mathbf{F}_R}{S_R - S_L}$$

the following integral averages are introduced:

$$\mathbf{U}_{*L} = \frac{1}{T(S_* - S_L)} \int_{TS_L}^{TS_*} \mathbf{U}(x,T)dx$$

$$\mathbf{U}_{*R} = \frac{1}{T(S_R - S_*)} \int_{TS_*}^{TS_R} \mathbf{U}(x,T)dx$$

The HLLC approximate Riemann solver is given as follows:

$$\widetilde{\mathbf{U}}(x,t) \begin{cases} \mathbf{U}_L & ,if \quad \frac{x}{t} \le S_L, \\ \mathbf{U}_{*L} & ,if \quad S_L \le \frac{x}{t} \le S_*, \\ \mathbf{U}_{*R} & ,if \quad S_* \le \frac{x}{t} \le S_R, \\ \mathbf{U}_R & ,if \quad \frac{x}{t} \ge S_R, \end{cases}$$

Now, the corresponding HLLC numerical flux can be displayed with the intermediate fluxes $\mathbf{F}_{*L}$ and $\mathbf{F}_{*R}$:

$$\mathbf{F}_{i+\frac{1}{2}}^{hllc} \begin{cases} \mathbf{F}_L & ,if \quad 0 \le S_L, \\ \mathbf{F}_{*L} & ,if \quad S_L \le 0 \le S_*, \\ \mathbf{F}_{*R} & ,if \quad S_* \le 0 \le S_R, \\ \mathbf{F}_R & ,if \quad 0 \ge S_R, \end{cases}$$

By integrating over appropriate control volume we are able to obtain:

$$\mathbf{F}_{*L} = \mathbf{F}_L + S_L(\mathbf{U}_{*L} - \mathbf{U}_L),$$

$$\mathbf{F}_{*R} = \mathbf{F}_{*L} + S_*(\mathbf{U}_{*R} - \mathbf{U}_{*L}),$$

$$\mathbf{F}_{*R} = \mathbf{F}_R + S_R(\mathbf{U}_{*R} - \mathbf{U}_R).$$

There are four unknown vectors, and we need to find the solution for the two intermediate fluxes $\mathbf{F}_{*L}$ and $\mathbf{F}_{*R}$. From above we can see that it is sufficient to find the solution for $\mathbf{U}_{*L}$ and $\mathbf{U}_{*R}$, but there are more unknowns than equations, so it is obvious that several conditions need to be restricted. To solve the algebraic problem, we impose for pressure and normal component of velocity:

$$\begin{cases} p_{*L} = p_{*R} = p_* \\ u_{*L} = u_{*R} = u_* \end{cases}$$

For tangential velocity components:

$$\begin{cases} v_{*L} = v_L, v_{*R} = v_R \\ u_{*L} = u_L, u_{*R} = u_R \end{cases}$$

For convenience, we set $S_* = u_*$, and by this if an estimate for S_* is solved out, the velocity component u_* of the star region is also known.

By those relations we have:

$$S_L \mathbf{U}_{*L} - \mathbf{F}_{*L} = \mathrm{S}_L \mathbf{U}_L - \mathbf{F}_L$$

$$S_R \mathbf{U}_{*R} - \mathbf{F}_{*R} = \mathrm{S}_R \mathbf{U}_R - \mathbf{F}_R$$

where all the right-hand sides of the both equations are known as constant vectors.

In the two star regions, assuming that S_L and S_R are known, we can obtain the following solutions for pressure:

$$p_{*L} = p_L + \rho_L (S_L - u_L)(S_* - u_L)$$

$$p_{*R} = p_R + \rho_R (S_R - u_R)(S_* - u_R)$$

As we imposed above, $p_{*L} = p_{*R}$, from this equation we can find the expression for the speed S_* with only the assumed S_L and S_R:

$$S_* = \frac{p_R - p_L + \rho_L u_L (S_L - u_L) - \rho_R u_R (S_R - u_R)}{\rho_L (S_L - u_L) - \rho_R (S_R - u_R)}$$

Now the problem become a simplified HLL solver. From relations above, the intermediate fluxes $\mathbf{F}_{*L}$ and $\mathbf{F}_{*R}$ can be expressed as

$$\mathbf{F}_{*K} = \mathbf{F}_K + S_K (\mathbf{U}_{*K} - \mathbf{U}_K)$$

in which K = L and K = R, with the intermediate states as

$$\mathbf{U}_{*K} = \rho \left(\frac{S_K - u_K}{S_K - S_*} \right) \begin{bmatrix} 1 \\ S_* \\ v_K \\ w_K \\ \frac{E_K}{\rho_K} + (S_* - u_K [S_* + \frac{p_K}{\rho_K (S_K - u_K)}]) \end{bmatrix}$$

and the final choice of the HLLC flux is

$$\mathbf{F}_{i+\frac{1}{2}}^{hllc} \begin{cases} \mathbf{F}_L & , if \quad 0 \le S_L, \\ \mathbf{F}_{*L} & , if \quad S_L \le 0 \le S_*, \\ \mathbf{F}_{*R} & , if \quad S_* \le 0 \le S_R, \\ \mathbf{F}_R & , if \quad 0 \ge S_R, \end{cases}$$

2.2.4 MUSCL–Hancock scheme

It is worth noting that using Godunov's method with piecewise constant data is only first order accurate in space. Based on the Godunov's theory, the direct application of a second order scheme unfortunately leads to spurious oscillations around discontinuities. There are two main approaches to improving the convergence rate; one is to use more information from the Riemann solution, as in the Weighted Average Flux method (Toro 1989), which allows for second-order accuracy. The other formulation, the MUSCL–Hancock scheme (van Leer 1984), the method van Leer attributes to S. Hancock, is an approach which achieves a second order extension of Godunov's method. By the reconstruction of the values crossing each cell boundary, the evolution of data by time steps and solving the Riemann problem, MUSCL-Hancock reconstruction allows for better second order accuracy than using piecewise constant values. In the next section, the total variation diminishing (TVD) version of MUSCL-Hancock is also introduced.

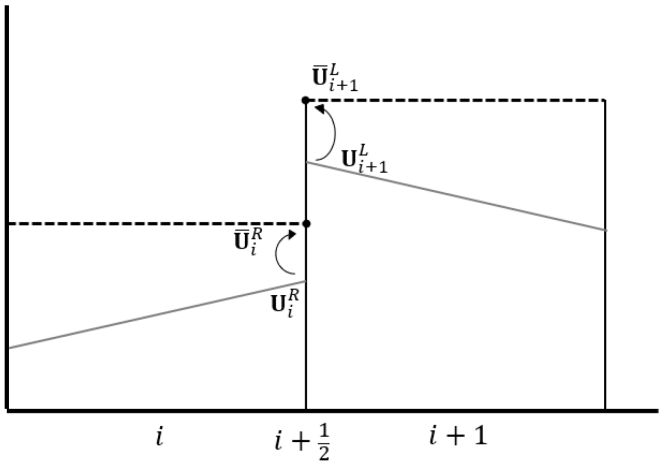

Figure 2.4 Advancement of boundary values of cell $\boldsymbol{U}_i^R$ and $\boldsymbol{U}_{i+1}^L$ to $\bar{\boldsymbol{U}}_i^R$ and $\bar{\boldsymbol{U}}_{i+1}^L$, and the Riemann problem solved at the intercell boundary $i+\frac{1}{2}$ in MUSCL-Hancock scheme,.

To reconstructing the data, defining the forward difference between nearby cells as:

$$\Delta\mathbf{U}_{i-\frac{1}{2}} = \mathbf{U}_i - \mathbf{U}_{i-1}$$

$$\Delta\mathbf{U}_{i+\frac{1}{2}} = \mathbf{U}_{i+1} - \mathbf{U}_i$$

Δ_i is a suitable slope vector of $\mathbf{U}_i(x)$ in cell$I_i = [x_{i-\frac{1}{2}}, x_{i+\frac{1}{2}}]$, defined as:

$$\Delta_i = \frac{1}{2}(1-\omega)\Delta\mathbf{U}_{i+\frac{1}{2}} + \frac{1}{2}(1+\omega)\Delta\mathbf{U}_{i-\frac{1}{2}}$$

where $\omega \in [-1,1]$.

The conservative variables at the left and right boundaries of the cell are obtained by the slope vector:

$$\mathbf{U}_i^L = \mathbf{U}_i - \frac{1}{2}\Delta_i$$

$$\mathbf{U}_i^R = \mathbf{U}_i + \frac{1}{2}\Delta_i$$

and are called the boundary extrapolated values.

For each cell, the left and right extrapolated values from the equation above are evolved by a half time step $\frac{1}{2}\Delta t$:

$$\bar{\mathbf{U}}_i^L = \mathbf{U}_i^L + \frac{1}{2}\frac{\Delta t}{\Delta x}[\mathbf{F}(\mathbf{U}_i^L) - \mathbf{F}(\mathbf{U}_i^R)]$$

$$\bar{\mathbf{U}}_i^R = \mathbf{U}_i^R + \frac{1}{2}\frac{\Delta t}{\Delta x}[\mathbf{F}(\mathbf{U}_i^L) - \mathbf{F}(\mathbf{U}_i^R)]$$

Noting that these advanced values $\mathbf{F}(\mathbf{U}_i^R)$ and $\mathbf{F}(\mathbf{U}_{i+1}^L)$ are the two fluxes of the left and right boundary states at each intercell position $i+\frac{1}{2}$, and they are then used as the input for a Riemann solver at each cell interface.

The only thing left to do is to solve the conventional piecewise constant data Riemann problem:

$$\mathbf{U}_t + \mathbf{F}(\mathbf{U})_x = 0$$

$$\mathbf{U}(x,0) = \begin{cases} \bar{\mathbf{U}}_i^R, & x < 0 \\ \bar{\mathbf{U}}_{i+1}^L, & x > 0 \end{cases}$$

2.2.5 TVD of MUSCL-Hancock scheme

To further suppress the oscillations and discontinuities, total variation diminishing (TVD) schemes are frequently utilized. The TVD version of MUSCL-Hancock scheme has a steady second-order accuracy in both time and space, and more importantly, it is oscillation free.

For the MUSCL reconstruction, the slope vector plays an important role in the scheme. One of the approaches to obtain the TVD version of MUSCL-Hancock, is to find a slope limiter $\phi(r)$, given by:

$$\overline{\Delta_i} = \phi(r)\Delta_i$$

where *r* is the ratio of slope at the surface of each cell, given by:

$$r = \frac{\Delta \mathbf{U}_{i-\frac{1}{2}}}{\Delta \mathbf{U}_{i+\frac{1}{2}}}$$

If $r < 0$, all limiters equal to zero (van Albada *et al.* 1982). If $r > 0$, With Δ_i given, this approach leads to the TVD region $\phi(r)$ given as follows:

$$0 \leq \phi(r) \leq \min[\phi_L(r), \phi_R(r)]$$

where

$$\begin{cases} \phi_L(r) = \dfrac{2\beta_{i-\frac{1}{2}} r}{1-\omega+(1+\omega)r} \\ \phi_R(r) = \dfrac{2\beta_{i+\frac{1}{2}} r}{1-\omega+(1+\omega)r} \end{cases}$$

and

$$\beta_{i-\frac{1}{2}} = \frac{2}{1+c}, \beta_{i+\frac{1}{2}} = \frac{2}{1-c}$$

where $\beta_{i-\frac{1}{2}}$ and $\beta_{i+\frac{1}{2}}$ are coefficients from the scalar case and *c* is the Courant number for a single wave present. Usually $\beta_{i-\frac{1}{2}}$ and $\beta_{i+\frac{1}{2}}$ are simply set as 1, giving a smaller TVD region. This is valid for all Courant numbers $|c| \leq 1$.

In the TVD MUSCL-Hancock scheme, there is a variety of slope limiters, i.e., the minmod, double minmod, superbee, van Albada, and van Leer limiters. Most of the limiters are defied by a 1-D constant coefficient equation, and all the slope limiters must fulfill the TVD condition:

$$\phi(r) \leq \min\left(\frac{4r}{1+r}, \frac{4}{1+r}\right), \qquad r \geq 0$$

In this study, we choose the van Leer limiter as the slope limiter. It is defined by:

$$\phi(r) = \begin{cases} 2\dfrac{\min(1,r)}{1+r}, & r > 0 \\ 0, & \text{otherwise} \end{cases}$$

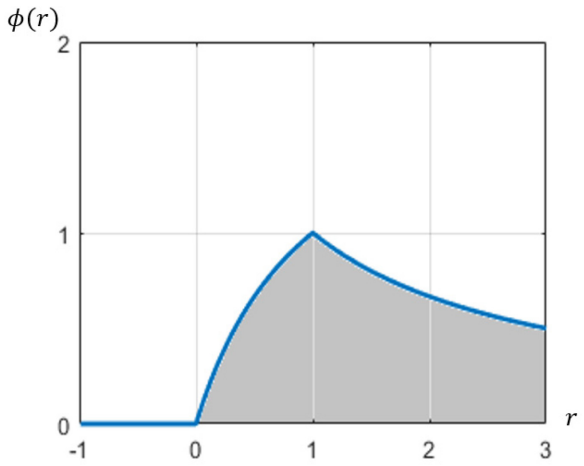

Figure 2.5 The van Leer limiter used in the MUSCL-Hancock scheme (grey)**.**

2.3 Computational time steps

To ensure positivity of the reconstructed pressure, the flux update formula is stable for time steps which satisfy the inequality:

$$\frac{\Delta t}{\Delta x}\max_i(S) < 1$$

where $\max_i(S)$ denotes the maximum wavespeed on the grid, which means that a signal cannot propagate more than one cell in a single time step. Alternatively, this condition can be re-arranged to obtain the time step:

$$\Delta t = \mathrm{C}_{CFL}\frac{\Delta x}{S^n_{\max}}$$

where Δx is the spatial discretization length and $S^{(n)}_{\max}$ the largest wave speed present at time level *n*, which means no wave present in the solution of all Riemann problems in this level *n* travels more than a distance of Δx in time Δt. For time-dependent, one-dimensional Euler equations:

$$S^n_{\max} = \max\{\left|S^L_{i+\frac{1}{2}}\right|, \left|S^R_{i+\frac{1}{2}}\right|\}$$

For $i = 0,1,\ldots\ldots,M$, $S^L_{i+\frac{1}{2}}$ and $S^R_{i+\frac{1}{2}}$ are the wave speeds of the left and right waves presented in the solution of Riemann problem. For multi-dimensional problem, this method of estimating is not reliable and the alternative is:

$$S_{\max}^{n} = \max\{|u_i^n| + a_i^n\}$$

Only data of the particle velocity u_i^n and sound speed a_i^n are used. To satisfy the time-step stability condition, the CFL (Courant, Friedrichs, Lewy) coefficient should be chosen before beginning the simulations in the range $0 < \mathrm{C_{cfl}} < 1$. The closer the coefficient is to 1, the more efficient the time matching scheme is. In this study we set the CFL coefficient as 0.9.

$$\Delta t = \mathrm{C}_{CFL} \frac{\Delta x}{S_{\max}^{n}}$$

$$S_{\max}^{n} = \max\{|u_i^n| + a_i^n\}$$

2.4 CUDA

In this study, the entire flow solver is implemented with CUDA programming language and computing platform, and running on a NVIDIA Tesla K40 General Purpose Graphics Processing Unit (GPGPU). Application of the GPU-CPU framework improves significantly the computational performance allowing high grid resolution simulations and parametric study to be performed efficiently. With CUDA, the solutions for all cells are computed separately by each single thread of the GPU, with those threads being logically bonded together into blocks and each block components around 64 threads so as to maintain capability for inter-thread communication. Up to 512 threads could be executed in parallel on the GPU. By executing multiple blocks at the same time, the GPU is able to “swap” between blocks and blocks in order to hide memory delay.

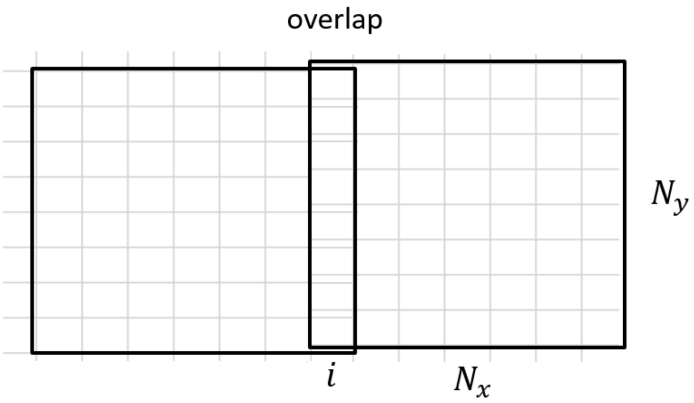

Figure 2.6 Implementation of the Riemann solver using the thread and block configuration with a one-cell overlap between blocks (Morgan 2013).

To connect all the blocks for the Riemann flow solver, an overlapping cell at the end of each block is required in the solver, as shown in **Figure 2.6** (Morgan 2013). Cells loaded with data $\mathbf{U}_{i-1}$, $\mathbf{U}_i$, and $\mathbf{U}_{i+1}$ reconstruct $\overline{\mathbf{U}}_i^L$ and $\overline{\mathbf{U}}_i^R$. Then, the i^{th} cell computes the flux $\mathbf{F}_{i-\frac{1}{2}}$, using the values from reconstructed cell $i-1$ and i. The overlap cannot be computed at the left side of the first block since there is no data available at the left front.

Therefore, the number of blocks that is enough for covering the whole computational system with a designated overlap can be determined by:

$$\text{blocks} = 1 + [\frac{\text{grid cells}}{\text{block width} + \text{overlap}}]$$

2.5 Code validation

2.5.1. One-dimensional Sod shock tube problem

An often used standard test to verify the accuracy of a certain approximate Riemann solver in the Riemann problem is the Sod shock tube problem. We select one test problem for the one-dimensional, time dependent Euler equations for ideal gases with $\gamma = 1.4$. In the chosen condition, the left state $\rho_L = 1.0, u_L = 0.75, p_L = 1.0$ and the right state $\rho_R = 0.125, u_R = 0.0, p_R = 0.1$. The two sides are separated by a

discontinuous point at the position $x = x_0$. The exact and simulated solutions can be found in the domain $0 \leq x \leq 1$ and there is 100 cells in the domain. Courant number coefficient is $C_{CFL} = 0.9$; boundary conditions are set as transmissive.

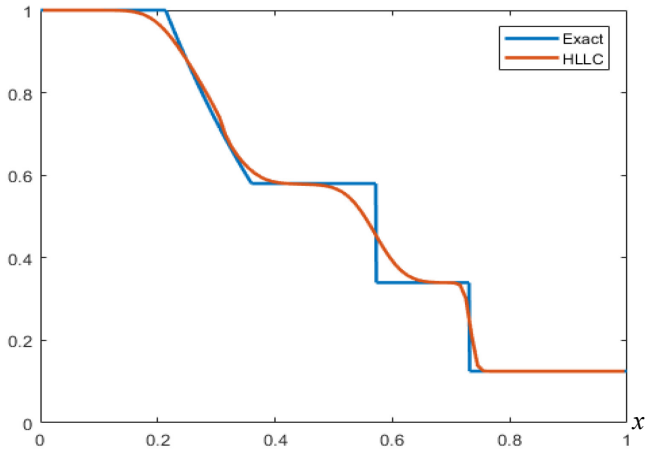

(a) Density

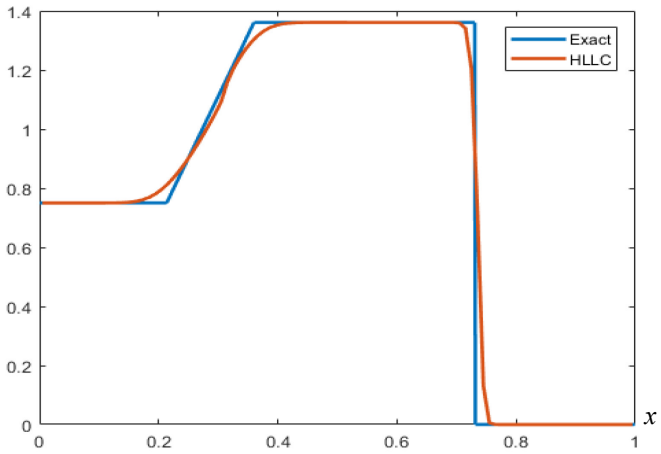

(b) Velocity

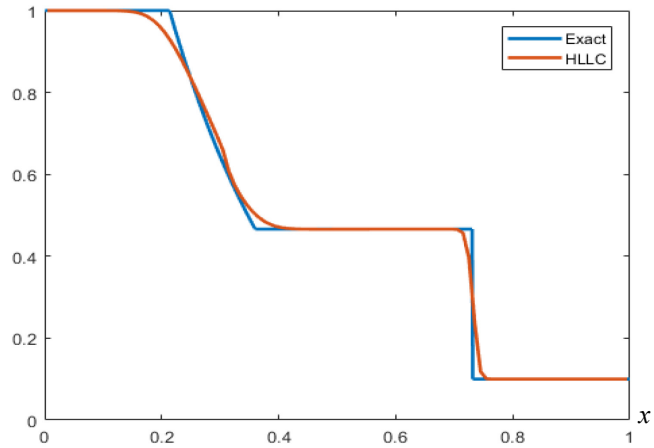

(c) Pressure

Figure 2.7 Comparison of the exact and approximate solution of the Sod shock tube problem.

In **Figure 2.7**, a shock wave at the right-hand side, a central discontinuity in the middle and a left sonic rarefaction wave can be found. The solution has considerable accuracy, showing the general trends in the process and the accurate values for each stage. The right shock wave, which is located at around x =0.7, is compressive, causing very rapid and strong changes of physical parameters since $p^* \geq p_R$. The central discontinuity is located at around x =0.5. Pressure and velocity stay still at this section, whereas density across the contact surface has a significant change. Finally, the left rarefaction wave is located between x =0.1 and x =0.3. A roughly smooth transition of physical parameters can be observed due to $p^* \leq p_L$.

2.5.2. Two-dimensional structure of cellular detonation

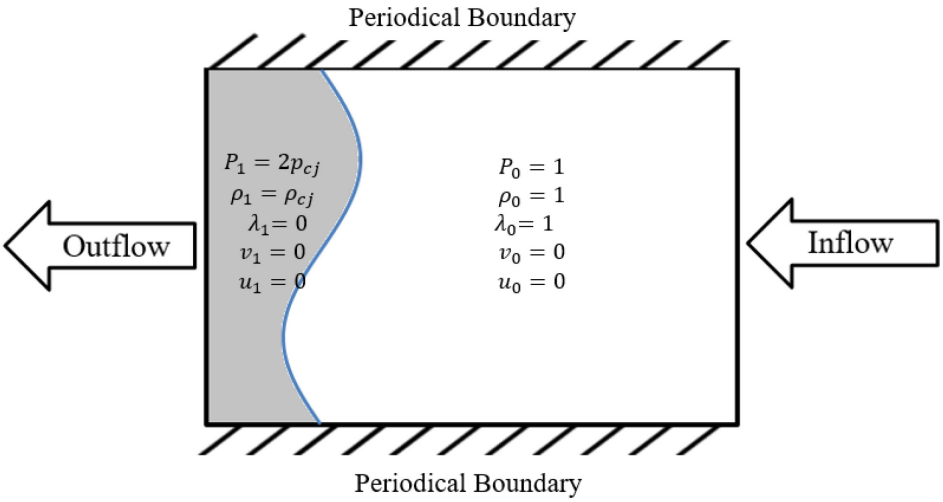

Figure 2.8 The initial and boundary conditions of the simulation

A two-dimensional numerical simulation of unsteady reactive flow using corrected boundary conditions in a 200 x 100 domain with 20 pts/$l_{1/2}$ is illustrated in **Figure 2.8**. In the left side of the domain, a sinusoidal surface divides the domain into two parts:

$$x = 5 \sin\left(\frac{2\pi}{100y}\right) + x_1$$

In the left-hand-side of the domain, a region of overpressure 2 P_{cj} causes a detonation wave propagating right forwards. The top and bottom boundaries are reflective

boundaries. At the right boundary, a constant inflow with the x-velocity D_{cj} is defined and the left boundary is relaxed by the inflow conditions (λ stays 0):

$$\mathbf{U}_{-1} = (1-r)\mathbf{U}_0 + r\mathbf{U}_{in}$$

$$\mathbf{U}_{-2} = (1-r)\mathbf{U}_1 + r\mathbf{U}_{in}$$

where $r = 0.05$ (Gamezo *et al.* 1999), $\mathbf{U}_{-1}$ and $\mathbf{U}_{-2}$ are ghost cells.

In this example, the initial condition is set as:

Table 1. Initial conditions for the cellular detonation simulation

Parameters	***Values***
Heat release, Q	50
Ratio of specific heats, γ	1.2
Initial Front position, x_I	50
Post-shock temperature, P_1	42.063
Post-shock density, ρ_1	1.795
CJ detonation pressure, P_{CJ}	21.531
CJ detonation Mach number, M_{CJ}	6.2162

Three cases of different groups of activation energy E_a and pre-exponential factor k are tested, relatively:

$$E_{a1} = 10, k_1 = 3.7$$

$$E_{a2} = 20,\ k_2 = 16.7$$

$$E_{a3} = 25,\ k_3 = 36.5$$

Soot foil is a common way to record the cellular structure of detonation in experiment. Numerically, to record the maxium pressure ever exsited at each grid cell is a way to reproduce the soot foil.

Figure 2.9 shows the numerical result of simulated soot for E_a = 20. The detonation is initiated with the early sinusoidal perturbation, and rapidly developes into a steady form of celluar detonation structure. The later pattern of the cellular structure is also shown. Despite the splitting and combinationof transverse waves, the pattern of the cells remains relatively regular. Thus, for this moderate activation energy case, the cellular detonation structure is moderately stable. With the exception of cases in which transverse waves split or combine, the size of cells is similar.

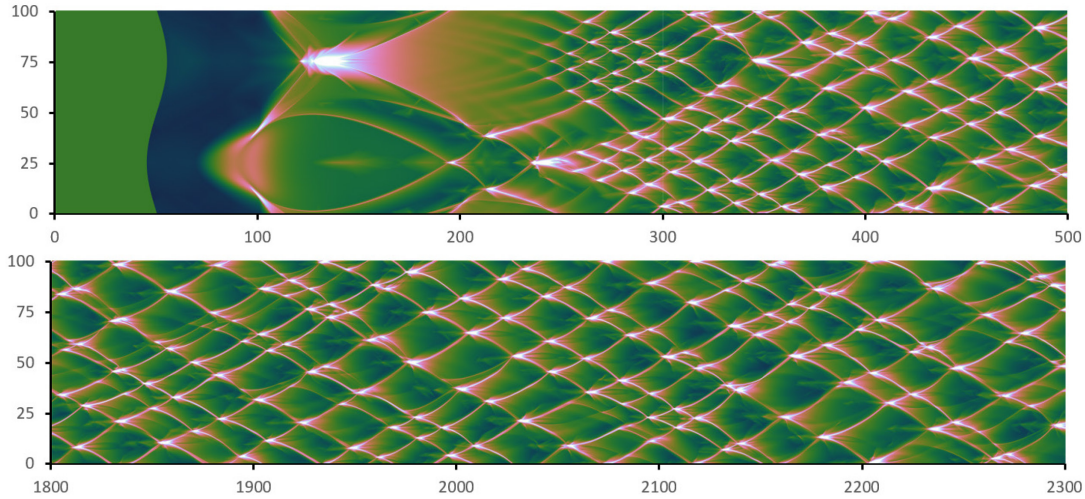

Figure 2.9 Numerical soot foil of $E_a = 20$. Upper is the result of early time showing the sinusoidal perturbation and the initiation of dettion; lower is the late cellular structure.

The numerical soot foils obtained with lower $E_a = 10$ and higher $E_a = 25$ are respectively shown in **Figure 2.10** and **Figure 2.11**. As we can see, for $E_a = 10$, the soot pattern is much more regular with more cells and the maxium pressure is also considerably lower. In contrast, soot foil at the high activation energy $E_a = 25$, is full of chaotic interactions with various waves interacting with each other and the maxium pressure is shown higher.

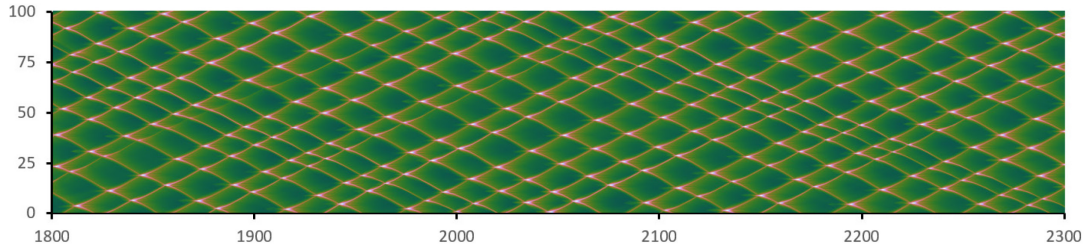

Figure 2.10 Numerical soot foil of $E_a = 10$ at late times, of which the cellular structure is regular.

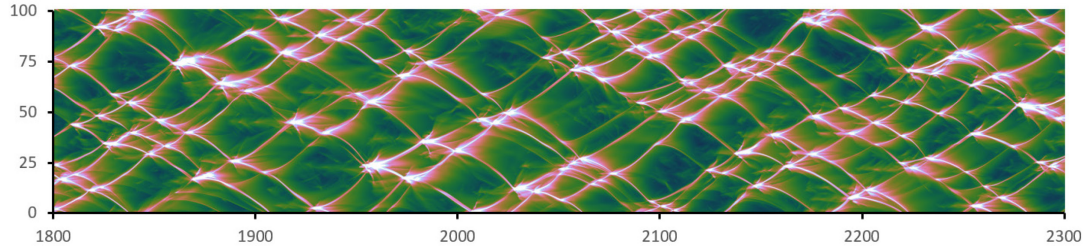

Figure 2.11 Numerical soot foil of $E_a = 25$ at late times, showing the irregular cellular structure.

Figure 2.12 also displays an images sequence of density schlieren plots showing the unstable detonation front of $E_a = 20$ at late times showing transverse waves

sweeping across the front and the generation of triple points and wave structure with incident, transverse waves and Mach stem.

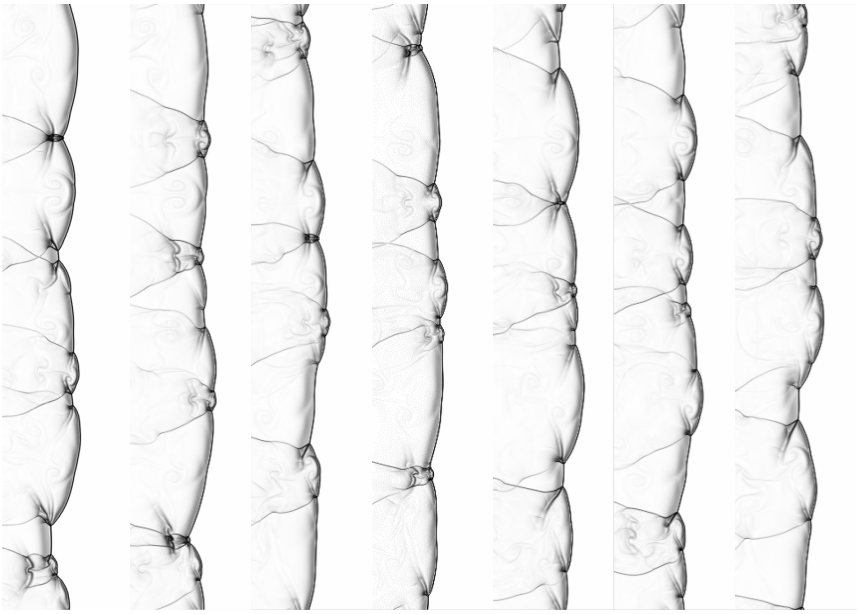

Figure 2.12 Density schlieren plots of the detonation structure development with $E_a = 20$.

2.6 Summary

In this chapter, the mathematical model and equations governing the two-dimensional detonation wave are presented. The applicability of the MUSCL-Hancock scheme to solve numerically the governing equations for the simulation is presented, improving the second order accuracy that Godunov scheme cannot apply to. Then we select HLLC approximate Riemann solver to solve this problem, which computes the intercell numerical flux directly, improving the efficiency of numerical simulation and the differences in result are generally negligible as compared to the exact Riemann solver. The stable time-integration algorithm is ensured by choosing the proper time step using the CFL number criterion. CUDA computing platform is used in this work to take full advantage of the computational resources, making sure it is not wasted and meanwhile maintain the accuracy of the resolutions. The numerical method is verified

by the one-dimensional Sod shock tube problem and simulation of the cellular detonation structure.

Chapter 3 Results and Discussion

In Chapter 2, the physical reactive flow model for detonation simulation and numerical methods are described. The numerical methodology is applied in this Chapter to look at the ODW phenomenon under different effects and particularly to carry out a parametric study to identify quantitatively the conditions of the two transition mechanism introduced in Chapter 1. To ensure the results are not affected by any numerical issue, a resolution and time-step study is also presented.

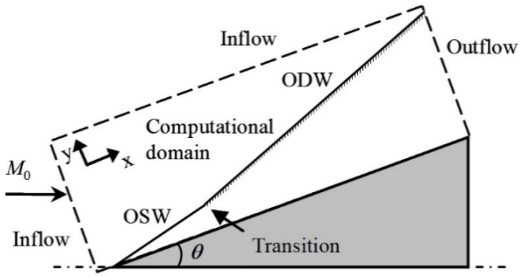

Figure 3.1 A schematic of the computational domain used for oblique detonation simulations.

3.1 Computational setup

The formation of a two-dimensional oblique detonation structure is induced by a supersonic incoming flow onto a wedge. The initial oblique shock transits into an oblique detonation surface after an induction period. To simulate ODW phenomena, the computational setup shown in **Figure 3.1** is used. The computational domain bounded by the dashed lines is rotated to the direction along the wedge surface. The Cartesian grid in this rectangular domain is thus aligned with the wedge surface and the inflow velocities to the computational domain are determined and projected based on the rotation angle. Inflow conditions are thus employed for the left and top boundaries; outflow conditions extrapolated from the interior are implemented on the right boundary and few grid cells before the wedge tip. Slip reflective boundary condition is used on the wedge surface.

Following previous canonical studies, e.g., Teng *et al.* 2014; Verreault *et al.* 2013;

Zhang *et al.* 2018; Grismer & Powers 1996, etc., the normalized heat release Q is chosen to be 50 and the isentropic exponent $\gamma = 1.2$ for both chemical kinetic models considered in this work. For the single-step Arrhenius model, the activation energy ranges between 5 and 60 in this work and k varies from 1.8 to 14,640, respectively. For the two-step kinetics, there are two associated activation energies, namely E_{I} and E_{R}, which are rescaled by the temperature jump across the leading shock of the detonation to give $\varepsilon_{\mathrm{I}} = 5.0T_{\mathrm{s}}$ and $\varepsilon_{\mathrm{R}} = 1.0T_{\mathrm{s}}$. The pre-exponential factor k_{R} is used in this work to change the reaction zone structure and varies from 1 to 10. Mixture parameters and corresponding ZND Chapman-Jouguet (CJ) detonation properties are provided in **Table 2.**

Table 2. Mixture parameters and corresponding CJ detonation properties

Parameters	***Values***
Heat release, Q	50
Ratio of specific heats, γ	1.2
Post-shock temperature, T_{s}	4.814
Post-shock temperature, P_{s}	42.063
Post-shock particle velocity, u_{vn}	0.7792
CJ detonation temperature, T_{CJ}	11.998
CJ detonation pressure, P_{CJ}	21.531
CJ detonation Mach number, M_{CJ}	6.2162

In this parametric study, three wedge angles θ and different inflow Mach number M_0. It is worth noting that the high E_a regime considered in this work has not been explored thoroughly in any previous studies due to the numerical resolution requirement. Boundaries separating the two aforementioned transition types are obtained and new features resulting from the effect of high activation energy on the flow structure in the vicinity of the ODW initiation region and the fully developed ODW unstable surface are discussed in detail.

To capture the complete ODW formation structure and to adjust the computational cost, different computational domains are used, i.e., 80 × 30, 160 × 60 or 220 × 80 for the one-step kinetics and 120 × 40, 150 × 50 for the two-step kinetic model, depending on the initial flow and mixture conditions. Three wedge angles θ are considered in this study, i.e., 26°, 28° and 30°.

3.2 Grid resolution study

An important numerical issue that we need to pay attention is that, in most of the former studies, a numerical resolution of 32 pts (or less) per characteristic reaction zone length of a CJ-ZND detonation($l_{1/2}$ and Δ_I for single- and two-step kinetic model, respectively) is used in computations. However, when activation energy reaches a higher value or the heat release rate becomes steep, a much higher numerical resolution is required to achieve "converged" solutions (Verreault *et al.* 2013; Teng *et al.* 2014). **Figure 3.2** shows the different temperature contours for the case of $M_0 = 12.5$, $\theta = 26°$ and high $E_a = 60$ for the one-step Arrhenius model with increasing grid resolutions from 32, 64 to 128 pts per half reaction zone length. It is clear that from **Figure 3.2** for $E_a = 60$, 32 grid points per half reaction zone length is insufficient. The fore part of the unstable ODW structure and the Kelvin Helmholtz (K-H) vortex-rolling along the shear layer cannot be revolved. Only when the resolution is increased to 64 pts per half reaction zone length, the global features converge as those compared well with the results obtained using 128 pts. Taking this issue into account, the default resolution considered in this work is 64 pts per half reaction zone length for E_a less than 30 and only for higher E_a values a grid resolution of 128 pts/$l_{1/2}$ is used. Equivalently, a resolution study result is also provided in **Figure 3.3** for the two-step induction-reaction kinetics for the case of $M_0 = 10.0$, $\theta = 30°$ and $k_R = 2.8$. For a more quantitative comparison, the pressure and temperature profiles along the line $y = 5$ are shown in **Figure 3.4**. Overall, the curves are overlapped together so the effects of different grids are indeed found negligible. These results confirm again that a resolution of 64 pts per ZND induction zone length is sufficient.

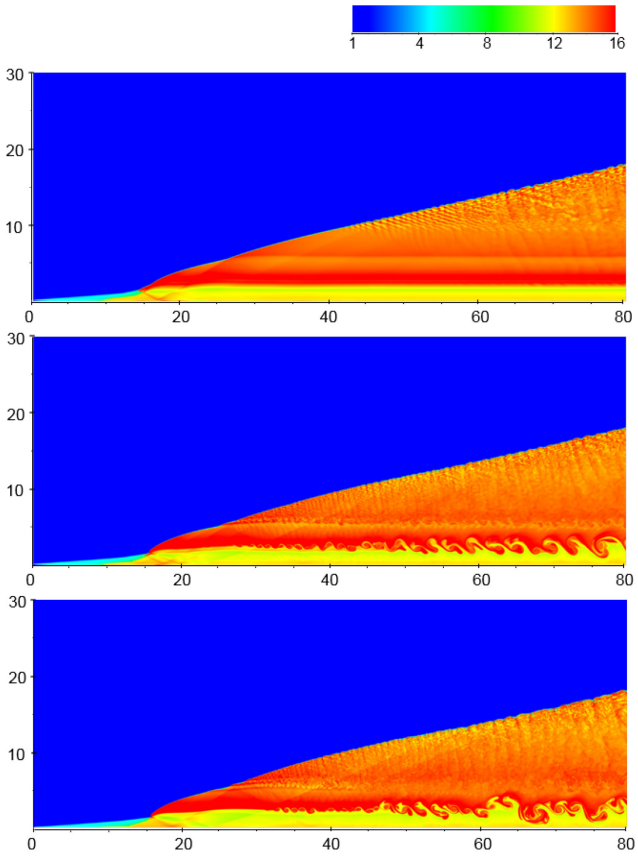

Figure 3.2 Temperature contours with 32 (upper), 64 (middle) and 128 (lower) pts/$l_{1/2}$ for M_0 = 12.5, θ = 26° and E_a = 60 for the one-step Arrhenius kinetics with k = 14,640.

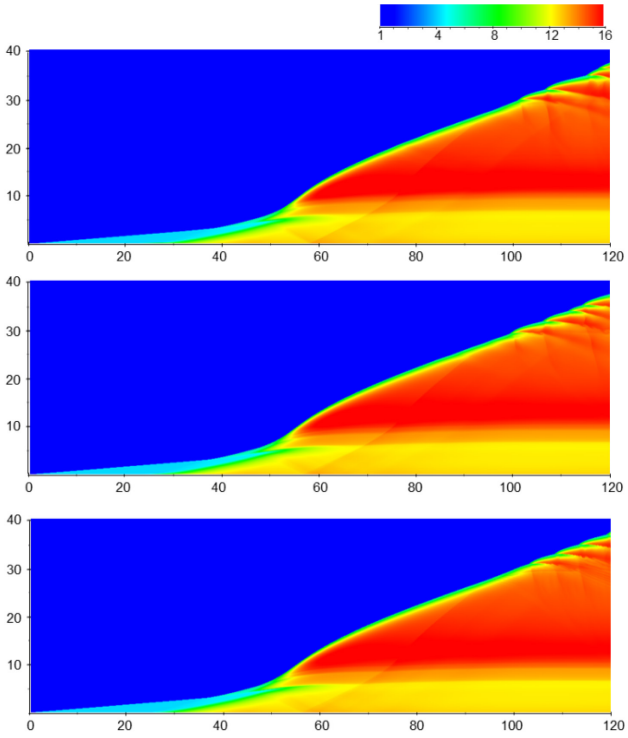

Figure 3.3 Temperature contours with 32 (upper), 64 (middle) and 128 (lower) pts/Δ_I for M_0 = 10.0, θ = 30° and k_R = 2.8 for the two-step induction-reaction kinetics.

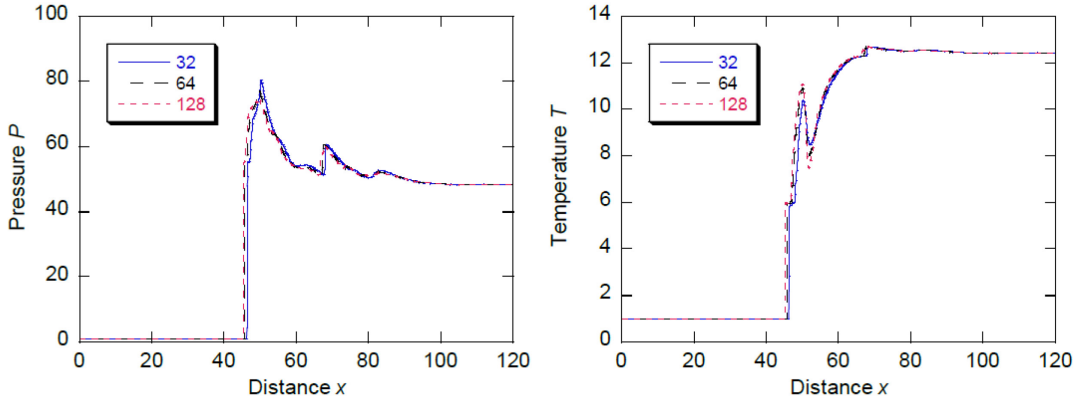

Figure 3.4 Pressure (left) and temperature (right) profiles along the line $y = 5$ obtained using different grid resolutions with $M_0 = 10.0$, $\theta = 30°$ and $k_R = 2.8$ for the two-step induction-reaction kinetics.

3.3 The effect of CFL number

Besides effects of numerical resolution, studies have shown that it is also important to take into consideration the accumulation of errors from each time-integration step for reactive flow simulations (Smirnov & Altoukhov, *et al.* 2014; Smirnov *et al.* 2015). In other words, the effect of time-step size needs also to be verified on the reliability of the results. Therefore, simulations with different numbers of time steps by varying the Courant-Friedrichs-Lewy (CFL) number (i.e., reducing the CFL number to 0.50 and 0.25) are performed for cases with both one-step Arrhenius kinetics and two-steps induction-reaction models, see **Figure 3.5** and **Figure 3.6**. It can be observed from the comparison, together with **Figure 3.2** and **Figure 3.3**, that the overall flow fields such as the wave structure around the initiation region and the location of the onset of ODW are not affected by the CFL number variation. Hence, the default CFL number of 0.90 was applied for all the following simulations.

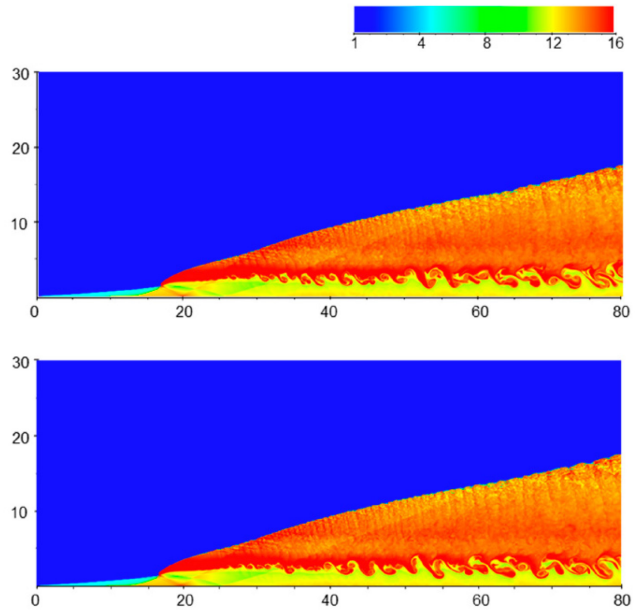

Figure 3.5 Temperature contours for the case $M_0 = 12.5$, $\theta = 26°$ and $E_a = 60$ obtained using the one-step Arrhenius kinetics with $k = 14{,}640$ and CFL number equal to 0.5 (upper); and 0.25 (lower)

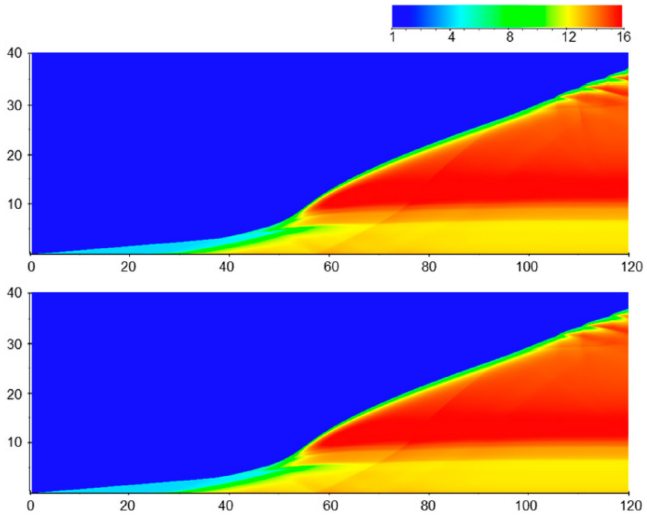

Figure 3.6 Temperature contours for the case $M_0 = 10.0$, $\theta = 30°$ and $k_R = 2.8$ using the two-step induction-reaction kinetics and CFL number equal to 0.5 (upper); and 0.25 (lower).

3.4 The effect of E_a in single-step Arrhenius model

Figure 3.7 first shows the ODW formation structures obtained with $\theta = 26°$, $M_0 = 12.5$ and 10, and $E_a = 35$ for the one-step Arrhenius kinetic model. Consistent with the

finding in the literature, the transition is characterized by a smoothly curved shock at M_0 = 12.5, while at low Mach number the transition is given by the classical abrupt structure. For the case with M_0 = 10, the multi-wave point connecting the deflagration wave, induction OSW, ODW and transverse compression waves can be clearly seen. A slip line extending downstream from the abrupt point can also be observed. Equivalently, **Figure 3.8** elucidates the two types of transition with a fixed inflow M_0 = 10 and θ = 26° but with various activation energies E_a from 20 to 30. Clearly, these results demonstrate that not only the inflow condition controls the transition process, the chemical sensitivity is another dominant parameter on the initiation evolution. The smooth transition can be achieved only by a mixture with very low temperature sensitivity (or equivalently a small E_a).

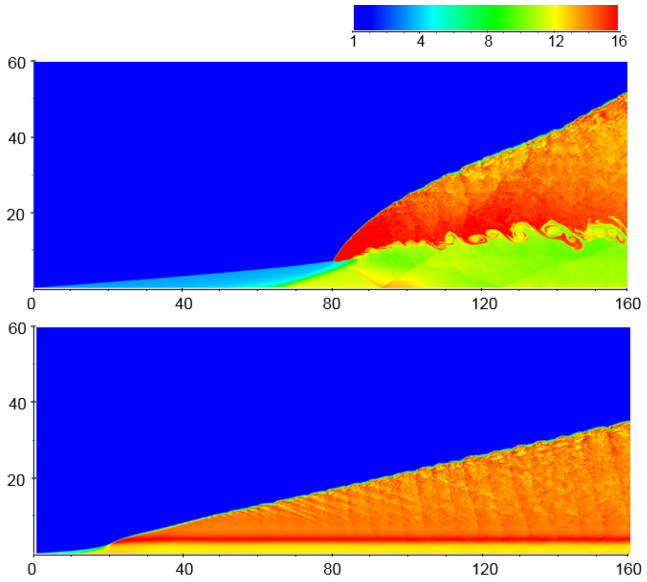

Figure 3.7 Temperature contours with E_a = 35, k = 185.0 and θ = 26° for M_0 = 10 (upper) and M_0 = 12.5 (lower).

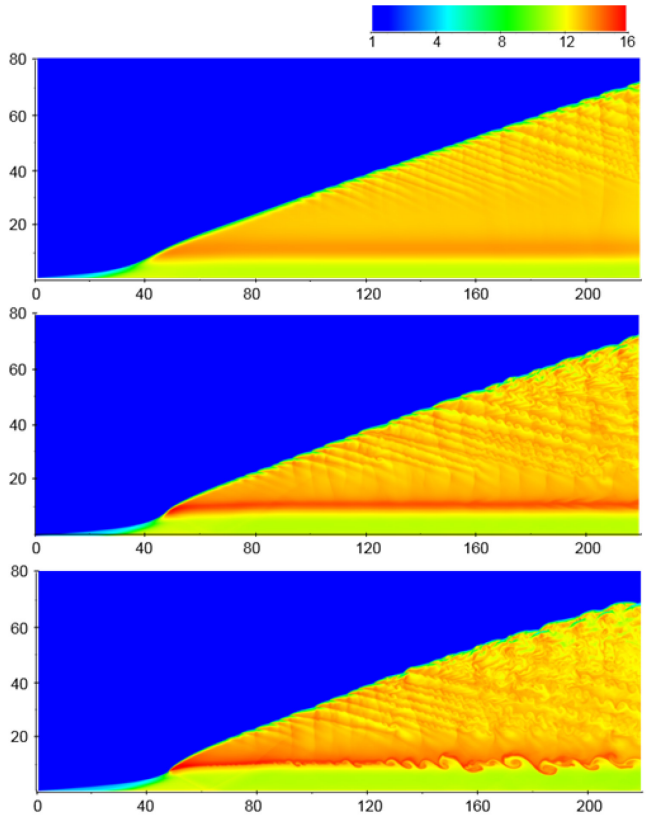

Figure 3.8 Temperature contours with $M_0 = 10$ and $\theta = 26°$ for $E_a = 20$ (upper) 24 (middle) and 30 (lower). The corresponding pre-exponential constant k values are 16.6, 31.0 and 81.1, respectively.

3.5 The effect of k_R in two-step induction-reaction kinetic model

Using the one-step Arrhenius kinetic model, the activation energy E_a controls the temperature sensitivity of the reaction rate. To examine the effect of the reaction zone length scale, a parametric study is carried out using the two-step induction-reaction kinetic model. The pre-exponential factor, k_R, is varied to probe how the ODW formation is affected by the heat release length. Results are presented in **Figure 3.9** for three different k_R values. It is also found that by increasing k_R, and hence, shortening the heat release length, the resulting ODW formation transits from a smooth to an abrupt configuration. Hence, not only the temperature sensitivity of the reaction zone plays a

role in determining the transition type, the heat release length represents another important factor.

Similar to **Figure 3.7**, **Figure 3.10** illustrates a similar trend of the effect of inflow Mach number for a mixture governed by induction-reaction kinetics. The two transition types are also observed by changing the Mach number from 9 to 11 with a fixed k_R = 2.5 and θ = 30°. At low Mach number M_0 = 9, the transition pattern is abrupt. For the case with M_0 = 10, the multi-wave wave point composing the deflagration wave, induction OSW, ODW and transverse compression waves is clear and the transition pattern is of a intermediate state. At M_0 = 11, the transition becomes a smooth curve.

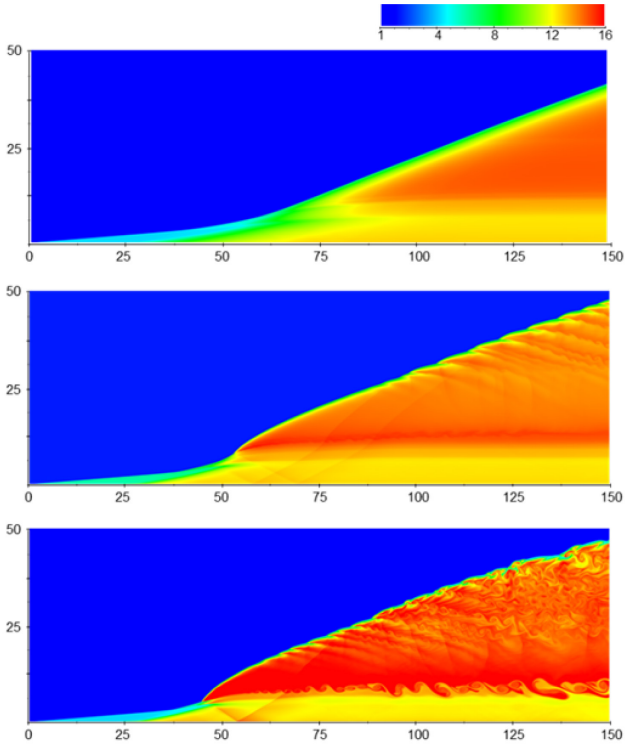

Figure 3.9 Temperature contours with M_0 = 10 and θ = 30° for k_R = 1.0 (upper); 2.98 middle); and 5.0 (lower).

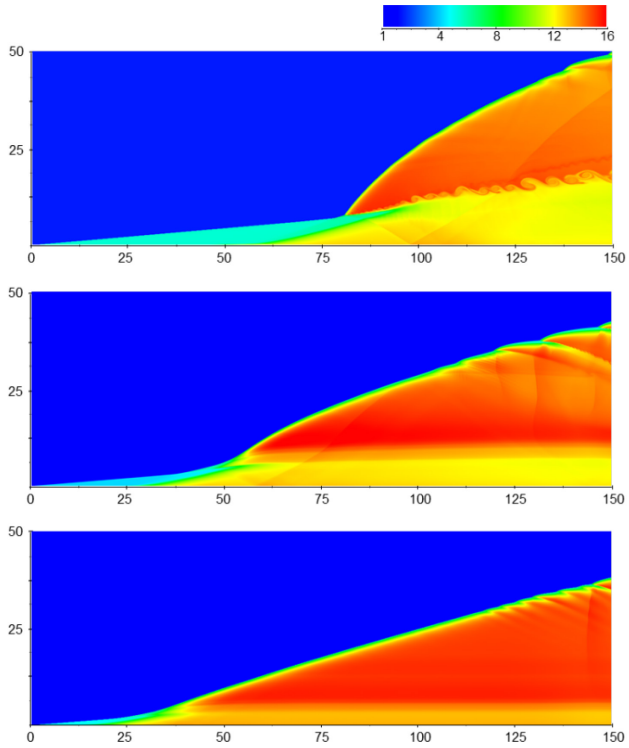

Figure 3.10 Temperature contours with $k_R = 2.5$ and $\theta = 30°$ for $M_0 = 9.0$ (upper); 10.0 (middle); and 11.0 (lower).

3.6 Critical values for transition

By carrying a full parametric study boundary curves in $E_{a,cr} - M_0$ and $k_{R,cr} - M_0$ spaces distinguishing the two types of OSW-ODW transition for different wedge angle θ are obtained. These curves are shown in **Figure 3.11** and **Figure 3.12** for the one-step Arrhenius and two-step induction-reaction kinetic models, respectively.

In **Figure 3.11**, it is observed that for all wedge angles θ a nearly linear relationship in most part between lower M_0 regime and the corresponding critical transition $E_{a,\,cr}$ is achieved. Only at high M_0 regime, the curve for the high wedge angle $\theta = 30°$ begins to deviate prominently. It can be observed from this plot that, at low M_0 regime, all three curves collapse, i.e., the critical $E_{a,cr}$ for the transition is independent of the wedge angle. In other words, the chemical kinetics is thus the controlling factor on the transition pattern of the ODW. As Mach number increases to very high values, the

boundary curves for the three wedge angles deviate from each other. This can be explained by the fact that at high M_0 regime, the resulting overdrive effect by the presence of the wedge with greater angles θ becomes the dominant factor on the transition type.

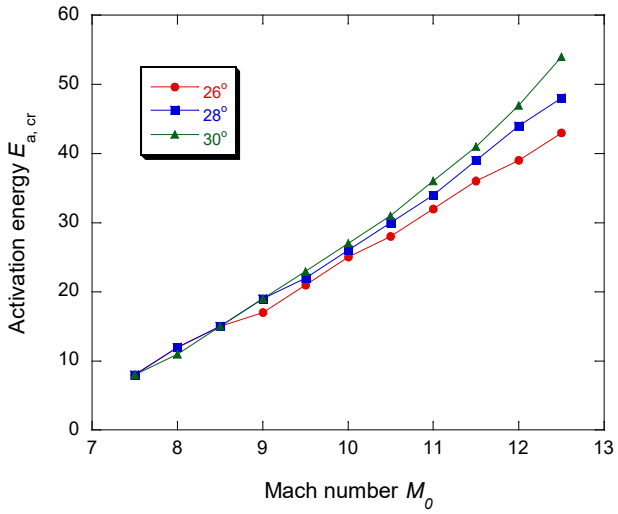

Figure 3.11 The conditions for smooth and abrupt transitions below and above the boundary respectively in the $E_{a,cr} - M_0$ plane for three different wedge angles θ.

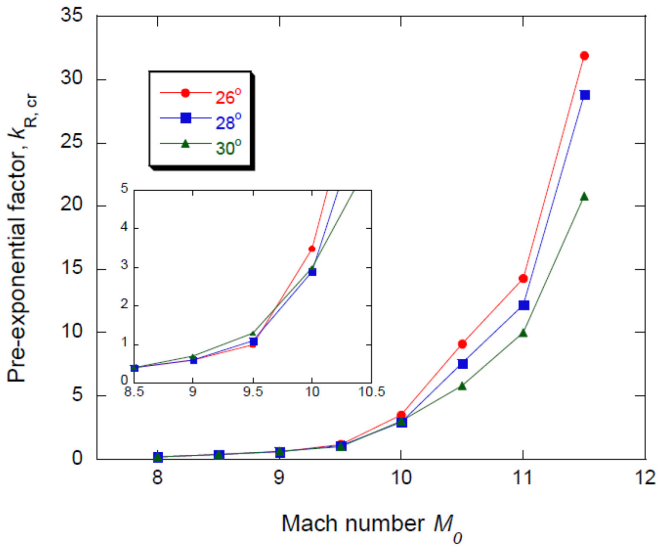

Figure 3.12 The conditions for smooth and abrupt transitions below and above the boundary respectively in the $k_{R,cr} - M_0$ plane for three different wedge angles θ.

Similar trend is also observed in **Figure 3.11** showing the boundary in $k_{R,cr} - M_0$ space. At low Mach number regime, all curves for different angles are close to each

other. The transition occurs at small k_R, i.e., at relatively larger heat release length. As the inflow Mach number increases, $k_{R,cr}$ increases exponentially and again, the three curves start to deviate from each other. This deviation at high Mach number regime and increasing angles can be again explained as a result of the overdriving effect becoming the dominant mechanism underlying the transition type.

In order to quantify the deviation of the results between different wedge angles with increasing Mach number, considering the lowest wedge angle θ = 26° as the baseline case the percentage difference of the critical values $E_{a,cr}$ and $k_{R,cr}$ between it and results with increasing wedge angle, i.e., θ = 28° and 30° are plotted in **Figure 3.13**. It appears the deviation begins at about M_0 = 9.0 in both cases with one-step Arrhenius kinetics and two-step induction-reaction kinetics. Below this critical Mach number, the boundaries are indeed the same for all wedge angles at the low Mach number regime.

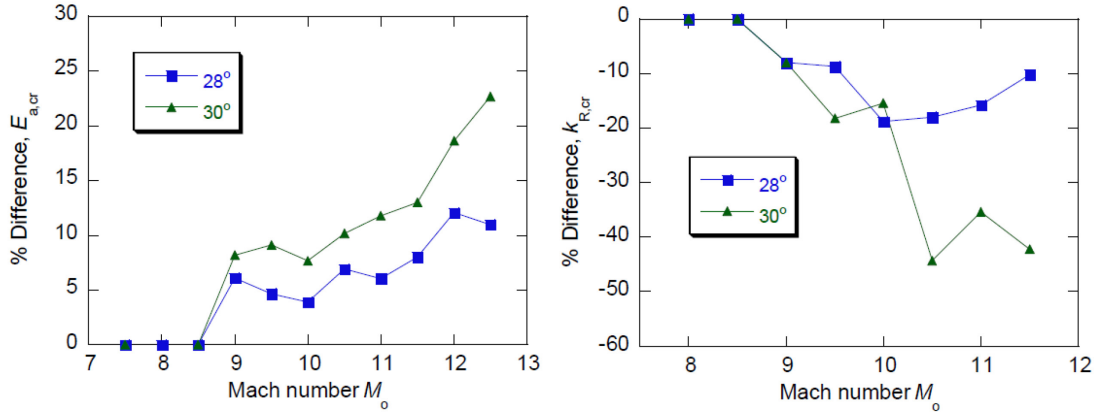

Figure 3.13 The percentage difference of $E_{a,cr}$ (left); and $k_{R,cr}$ (right) between the base case of θ = 26° and increasing wedge angles θ = 28° and 30°.

3.7 Overdrive degree

For a normal detonation in a tube, the velocity of the shock front D should be no less than the velocity of corresponding CJ detonation D_{cj}. The parameter overdrive degree, commonly defined as $f = (D/D_{cj})^2$, can also be determined as:

$$f = (\frac{M_0 \cdot sin\beta}{M_{cj}})^2$$

where β and M_{CJ} are the oblique detonation angle and Mach number of the CJ detonation for a given Q and γ. To obtain the overdrive degree, the oblique detonation wave angle β should be calculated first with the given Mach number M_0 and wedge angle θ, from the detonation shock polar relation:

$$\frac{\tan\beta}{\tan(\beta-\theta)} = \frac{(\gamma+1)M^2\sin^2\beta}{\gamma M^2\sin^2\beta + 1 - \sqrt{(M^2\sin^2\beta-1)^2 - 2(\gamma^2-1)M^2\sin^2\beta\cdot(\frac{Q}{\gamma})}}$$

For Q = 50 and γ = 1.2, the initial Mach numbers, the wedge angles and the corresponding overdrive degrees are respectively tabulated in **Table 3**. In fact, it is known that the heat release length scale has an effect on the instability of detonation, i.e., the shorter the heat release length, the more sensitive the detonation wave to flow perturbation. First, by keeping the same level of temperature sensitivity, i.e., same activation energies for both the induction and reaction steps, overall the higher Mach number and wedge angle have a stabilizing effect by reducing the overall temperature sensitivity of the reaction. Hence, a much greater value of k_R thus tends to reduce the heat release length and cause the transition from a smooth to an abrupt formation type. Second, for increasing overdrive, the temperature in the induction region is higher. This in turn increases the subsequent heat release rate in the reaction zone and shortens the heat release length. This provides a possible explanation why the critical k_R decreases for increasing wedge angle at the high Mach number regime due to the increase of f.

Table 3. Degree of overdrive f for different inflow Mach number M_0 and wedge angle θ

M_0	θ	f
9	26	1.20
9	28	1.27
9	30	1.36
12	26	1.50
12	28	1.63
12	30	1.77

3.8 Other ODW features

In a number of previous studies on ODW, the high Mach number inflow regime and a one-step Arrhenius kinetic model with low to moderate E_a are considered. In fact, by further increasing E_a in a high M_0 regime, the ODW flow field becomes more unstable, thus giving rise to more complex features. **Figure 3.14** shows the results obtained for $\theta = 26°$ and $M_0 = 12.5$ with a large activation energy $E_a = 60$, under which the transition is of an abrupt type. In the limit of large E_a, more instabilities begin to appear on the downstream fully-developed ODW surface. The increase of E_a makes the ODW cellular surface more irregular. For large E_a, the slip line also becomes unstable and the classical roll-up behavior of the K-H instability in the detonation product becomes more apparent. Similar to normal cellular detonation (Ng & Zhang 2012; Gamezo *et al.* 1999; Choi *et al.* 2008), for large E_a, the ODW cellular surface also becomes highly irregular with unburned pockets behind the leading ODW front (Choi *et al.* 2007; Teng *et al.* 2015; Gui & Fan 2012).

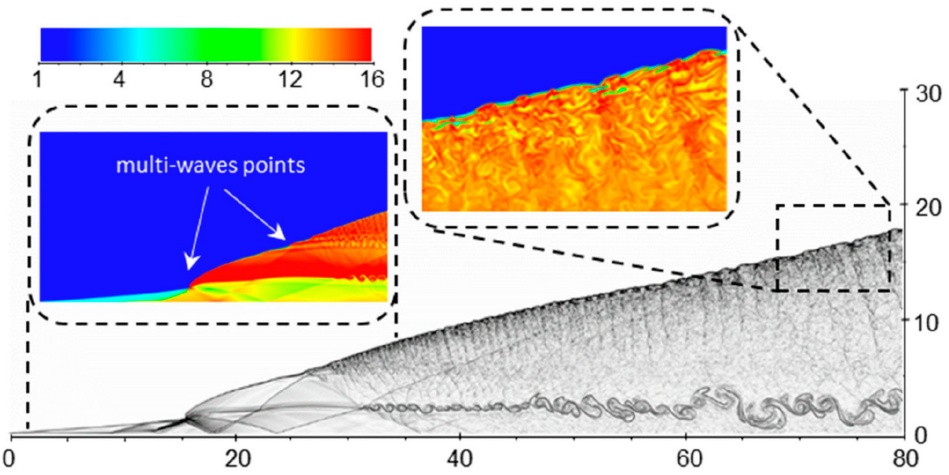

Figure 3.14 Schlieren plot and temperature contours (sub-plot) with 128 pts/$l_{1/2}$ for $M_0 = 12.5$, $E_a = 60$, $k = 14{,}640$ and $\theta = 26°$.

Another key feature is revealed near the initiation region. It is shown that the transverse compression wave resulting from the initiation point and reflected between

the wall and the slip line becomes stronger as E_a increases. The reflected compression wave from the wall further adjusts the gas parameters of the combustion products and penetrates the slip line, and influences the initially smooth ODW surface. The result of this interaction is the formation of another multi-wave point similar to the first initiation point. A second slip line, although faint, can be seen downstream, which eventually becomes unstable far downstream within the combustion product due to the K-H instability. At $E_a = 60$, this second multi-wave point appears to be close to the first appearance of transverse waves after another segment of smooth ODW from the main initiation location. For future works, computations taking into account viscous and diffusion effects by solving the Navier-Stokes equations (Mahmoudi *et al.* 2014, Ziegler *et al.* 2011) need to be considered in order to explore more quantitatively the aforementioned features obtained for large E_a such as the strong K-H instability along triple-point shear layers and the unstable oblique detonation cellular structure.

Chapter 4 Conclusions

4.1 Concluding remarks

In summary, this paper investigates the effects of chemical reaction kinetics on ODW initiation using high resolution numerical simulations. Two simplified kinetic models, namely, the conventional one-step Arrhenius kinetics over a wide range of activation energy E_a and the two-step induction-reaction kinetics are considered. The use of a GPU-based solver allows the simulations to be performed using high numerical resolution and a parametric study to be carried out efficiently. The present results obtained using a different computing platform further confirm the validity of the data obtained in previous studies using the conventional CPU computing. For the first time, this study provides quantitative results of the critical conditions distinguishing the two known ODW formation types in the $M_0 - E_a$ and $k_{R,cr} - M_0$ planes using the one-step Arrhenius and two-step models, respectively. At low Mach number regimes, all critical boundary curves with different wedge angles are close to each other, indicating that the transition is dominated by chemical kinetics. As inflow Mach number increases, the results for different wedge angles start to deviate from each other. This deviation can be explained by the fact that, at the high Mach number regime, the overdrive factor in turn plays a prominent role for determining the transition type. For the one-step Arrhenius case, flow features are revealed in finer details in the limit of large activation energy, including the presence of a second multi-wave point and the apparent rolled-up vortex instabilities in the combustion product along each slip line extending downstream from the multi-wave points near the initiation region.

4.2 Future work

For future works, as mentioned above, computations taking into account viscous and diffusion effects by solving the Navier-Stokes equations can be taken into consideration in order to explore the former results more quantitatively. Additional

simulation conditions using more complex chemical kinetic models and combustible thermo-parameters can be performed to research in more detailed realistic effect of chemistry. Other wedge geometries can be considered to facilitate the onset of oblique detonation wave transited from the initial oblique shock waves induced by the interaction between the incoming flow and wedge boundary. The effect of wedge surface morphology can also be analyzed on the initiation and stability of the oblique detonation waves. To mimic practical conditions, fluctuations on the incoming flow from the left boundary of the domain can be imposed and look at the stability and response of the ODW subject to the changing inflows.

For the numerical method itself, the current numerical framework can be further modified. Higher order schemes, higher resolutions and the viscous effects leading to the presence of boundary layer can be considered. Nevertheless, these aforementioned modifications demand higher requirement for scientific computing and computational optimization. Therefore more advanced programming and computer hardware are required to compliment these development. A better parallel CPU and GPU based computing strategy can also be further explored to accelerate the simulation running process.

References

1. Adelman, H.G., Cambier, J.L., Menees, G.P., Balboni, J.A. Analytical and experimental validation of the oblique detonation wave engine concept. *AIAA Paper* No. AIAA-88–0097, **1988**.
2. Alexander, D.C., Sislian, J.P. A computational study of the propulsive characteristics of a Shcramjet engine. *J. Propul. Power* **2008**, 24, 34–44.
3. Ashford, S.A., Emanuel, G. Wave angle for oblique detonation waves. *Shock Waves*. **1994**, 3, 327–329.
4. Austin, J.M. *The role of instabilities in gaseous detonation*, PhD thesis, California Institute of Technology, California, **2003**.
5. Austin, J.M.; Pintgen, F.; Shepherd, J.E. Reaction zones in highly unstable detonations. *Proc. Combust. Inst.* **2005**, 30, 1849-1857.
6. Berthelot, M. Sur la vitesse de propagation des phénomènes explosifs dans les gaz. *C.R. Acad. Sci. Paris* **1881**, 93, 18-22.
7. Berthelot, M., Vielle, P. L'onde explosive. *Ann. Chim. Phys.* **1883**, 28 (5), 289-332.
8. Betelin, V.B., Nikitin, V.F., Smirnov, N.N. Using GPUs for solving problems of combustion and physicochemical transformations. *Math Models Comput. Simul*. **2017**, 9, 727–741.
9. Bourlioux, A. *Numerical Study of Unstable Detonations*. PhD Thesis, Princeton University, Princeton, NJ, USA, **1991**.
10. Bourlioux, A., Majda, A.J. Theoretical and numerical structure for unstable two-dimensional detonations. *Combust. Flame* **1992**, 90, 211–229.
11. Cambier, J. L., Adelman, H., Menees, G. P. Numerical simulations of an oblique detonation wave engine. *J. Propul. Power*, **1990**, 6, 315–323.
12. Chan, J., Sislian, J.P., Alexander, D. Numerically simulated comparative performance of a Scramjet and Shcramjet at Mach 11. *J. Propul. Power* **2010**, 26, 1125–1134.
13. Chapman, D.L. On the rate of explosion in gases. In Philosophical Magazine, January **1899**, volume 47 of 5, pages 90-104. London: Taylor & Francis.
14. Choi, J. Y., Kim, D. W., I. Jeung, S., Ma, F., Yang, V. Cell-like structure of unstable oblique detonation wave from high-resolution numerical simulation. *Proc. Combust. Inst.* **2007**, 31, 2473–2480.
15. Choi, J.Y., Ma, F., Yang, V. Some numerical issues on simulation of detonation cell structures. *Combust. Expl. Shock Waves* **2008**, 44, 560–578.
16. Courant, R., Friedrichs, K.O. *Supersonic Flows and Shock Waves.* Interscience,

New York, USA, **1948**.

17. Da Silva, L.F.F., Desbordes, D., Deshaies, B. Stabilization of an oblique detonation wave by a wedge: A parametric numerical study. *Combust. Flame* **2000**, 121, 152–166.
18. Döring, W. On detonation processes in gases. *Ann. Phys.* **1943**, 43, 421-436.
19. Emanuel, G., Tuckness, D.G. Steady, oblique, detonation waves. *Shock Waves.* **2004**, 13, 445–451.
20. Erpenbeck, J.J. Stability of idealized one-reaction detonations. *Phys. Fluids* **1964**, 7(5), 684–696.
21. Erpenbeck, J.J. Stability of steady-state equilibrium detonations. *Phys. Fluids* **1962**, 5(5), 604–614.
22. Fickett, W., Davis, W.C. *Detonation*. University of California Press. Berkeley, CA, **1979.**
23. Fickett, W., Wood, W.W. Flow calculations for pulsating one‐dimensional detonations. *Phys. Fluids* **1966**, 9 (5), 903–916.
24. Fujiwara, T., Reddy, K.V. Propagation mechanism of detonation – three dimensional phenomena. *Mem. Fac. Eng. Nagoya Univ.* **1989**, 41, 1–18.
25. Gamezo, V.N., Desbordes, D., Oran, E.S. Formation and evolution of two-dimensional cellular detonations. *Combust. Flame* **1999**, 116, 154–165.
26. Grismer, M.J., Powers, J.M. Numerical predictions of oblique detonation stability boundaries. *Shock Waves* **1996**, 6, 147–156.
27. Gross, R.A., Oblique detonation waves. *AIAA J.* **1963**, 1, 1225–1227.
28. Godunov, S.K., A difference method for numerical calculation of discontinuous solutions of the equations of hydrodynamics, *Mat. Sb. (N.S.)*, **1959**, 47(89), 3, 271–306
29. Gui, M.Y., Fan, B.C., Dong, G. Periodic oscillation and fine structure of wedge-induced oblique detonation waves. *Acta Mech. Sin*. **2011**, 27, 922–928.
30. Gui, M.Y., Fan, B.C. Wavelet structure of wedge-induced oblique detonation waves. *Combust. Sci. Tech.* **2012**, 184, 1456–1470.
31. He, L.T., Lee, J.H.S. The dynamical limit of one-dimensional detonations. *Phys. Fluids* **1995**, 7 (5), 1151–1158.
32. Heiser, W. *Hypersonic Airbreathing Propulsion*; AIAA Education Series, AIAA, Washington, DC, USA, **1994**.
33. Hertzberg, A., Bruckner, A.P., Knowlen, C. Experimental investigation of ram accelerator propulsion modes. *Shock Waves* **1991**, 1, 17–25.
34. Higgins, A.J. Ram accelerators: Outstanding issues and new directions. *J. Propul.*

Power **2006**, 22, 1170–1187.

35. Higgins, A.J. Steady One-Dimensional Detonations. In *Shock Wave Science and Technology Library*; Zhang, F., Ed.; Springer: Berlin, Germany, Vol. 6, Chap. 2, **2012**.
36. Iwata, K., Nakaya, S., Tsue, M., Wedge-stabilized oblique detonation in an inhomogeneous hydrogen–air mixture. *Proc. Combust. Inst.* **2017**, 36, 2761–2769.
37. Jouguet, J. C. E. Sur la propagation des réactions chimiques dans les gaz. J. Math. Pures Appliquées **1905**, 1, 347–425.
38. Ju, Y., Masuya, G., Sasoh, A. Numerical and theoretical studies on detonation initiation by a supersonic projectile. *Proc. Symp. (Int.) on Combust.* **1998**, 27 (2), 2225–2231.
39. Ju, Y., Sasoh A., Masuya G. On the detonation initiation by a supersonic sphere. In: Takayama, K.; Sasoh, A. (eds) *Ram Accelerators*. Springer, Berlin, Heidelberg, **1998**.
40. Kailasanath, K. Recent developments in the research on pulse detonation engines. *AIAA J.* **2003**, 41, 145–159.
41. Kailasanath, K., E.S. Oran, J.P. Boris, Young, T.R. Determination of detonation cell size and the role of transverse waves in two-dimensional detonations. *Combust. Flame* **1985**, 61, 199–209.
42. Kaneshige, M.J., Shepherd, J.E. Oblique detonation stabilized on a hypervelocity projectile. *Proc. Symp. (Int.) on Combust.* **1996**, 26, 3015–3022.
43. Kaneshige, M., Shepherd, J.E. Detonation database. *GALCIT Tech. Rept. FM 97*, **1997** (Web page, http://www.galcit.caltech.edu/detn_db/html/db.html).
44. Kasahara, J., Fujiwara, T., Endo, T., Arai, T. Chapman-Jouguet oblique detonation structure around hypersonic projectiles. *AIAA J.* **2001**, 39, 1553–1561.
45. Lee, J.H.S. Initiation of detonation by a hypervelocity projectile. *Prog. Astronaut. Aeronaut.* **1997**, 173, 293–310.
46. Lee, J.H.S. *Detonation Phenomenon*; Cambridge University Press, New York, NY, USA, **2008**.
47. Lee, H.I., Stewart, D.S. Calculation of linear detonation instability: one-dimensional instability of planar detonations. *J. Fluid Mech.* **1990**, 216, 103–132.
48. Lefebvre, M.H., Oran, E.S. Analysis of the shock structures in a regular detonation. *Shock Waves* **1995**, 4, 277–283.
49. Lehr, H.F. Experiments on shock-induced combustion. *Astronaut. Acta* **1972**, 17, 589–597.
50. Li, C., Kailasanath, K., Oran, E.S. Detonation structure behind oblique shocks. *Phys. Fluids* **1994**, 6, 1600–1611.

51. Li, C., Kailasanath, K., Oran, E.S. Effects of boundary layers on oblique detonation structures. *AIAA Paper* **1993**, No. 93–0450.

52. Liu, Y., Han, X.D., Yao, S.B., Wang, J.P. A numerical investigation of the prompt oblique detonation wave sustained by a finite-length wedge. *Shock Waves*. **2016**, 26, 729–739.

53. Maeda, S., Kasahara, J., Matsuo, A. Oblique detonation wave stability around a spherical projectile by a high time resolution optical observation. *Combust. Flame* **2012**, 159 (2), 887–896.

54. Mallard, E., Le Châtelier, H. Recherches expérimentales et théorétiques sur la combustion des mélanges gazeux explosifs. *Ann. Mines* **1883**, 8 (4), 274–568.

55. Mahmoudi, Y., Karimi, R., Deiterding, R., Emami, S. Hydrodynamic instabilities in gaseous detonations: Comparison of Euler, Navier-Stokes, and large-eddy simulation. *J. Propul. Power* **2014**, 30, 384–396.

56. McVey, J.B., Toong, T.Y. Mechanism of instabilities of exothermic hypersonic blunt-body flows. *Combust. Sci. Tech.* **1971**, 3, 63–76.

57. Morgan, G. *The Euler equations with a single-step Arrhenius reaction*. MPhil thesis in scientific computing, University of Cambridge, UK, **2013**.

58. Morris, C.I., Kamel, M.R., Hanson, R.K. Shock-induced combustion in high-speed wedge flows. *Proc. Combust. Inst*. **1998**, 27, 2157–2164.

59. Ng, H.D., Lee, J.H.S. Comments on explosion problems for hydrogen safety. *J. Loss Prev. Proc. Ind.* **2008**, 21 (2), 136–146.

60. Ng, H.D., Radulescu, M.I., Higgins, A.J., Nikiforakis, N., Lee, J.H.S. Numerical investigation of the instability for one-dimensional Chapman–Jouguet detonations with chain-branching kinetics. *Combust. Theory. Model.* **2005**, 9, 385–401.

61. Ng, H.D., Zhang, F. Detonation Instability. In *Shock Wave Science and Technology Library*; Zhang, F., Ed.; Springer: Berlin, Germany, Vol. 6, Chap. 3, **2012**.

62. Oppenheim. A.K. Dynamic features of combustion. *Philosophical Transactions of the Royal Society of London A* **1985**, 315, 471–508.

63. Oran, E.S. Understanding explosions – From catastrophic accidents to the creation of the Universe. *Proc. Combust. Inst.* **2015**, 35(1), 1-35.

64. Oran, E.S., Kailasanath, K., Guirguis, R.H. Numerical simulations of the development and structure of detonations. *Prog. Astronaut. Aeronaut.* **1988**, 114, 155–169.

65. Oran, E.S., Young, T.R., Boris, J.P., Picone, J.M., Edwards, D.H. A study of detonation structure: The formation of unreacted gas pockets. *Proc. Combust. Inst.* **1982**, 19, 573–582.

66. Papalexandris, M.V. A numerical study of wedge-induced detonations. *Combust. Flame*. **2000**, 120, 526–538.

67. Pratt, D.T., Humphrey, J.W., Glenn, D.E. Morphology of standing oblique detonation waves. *J. Propul. Power* **1991**, 7, 837–845.

68. Radulescu, M.I. *The Propagation and Failure Mechanism of Gaseous Detonations: Experiments in Porous-Walled Tubes*. PhD thesis, McGill University, Montreal, Canada, **2003**.

69. Ren, Z., Wang, B., Xiang, G., Zhao, D., Zheng, L. Supersonic spray combustion subject to scramjets: Progress and challenges. *Prog. Aero. Sci.* **2019**, 105, 40–59.

70. Roy, G.D., Frolov, S.M., Borisov, A.A., Netzer, D.W. Pulse detonation propulsion: challenges, current status, and future perspective, *Prog. Energy Combust. Sci.* **2004**, 30, 545–672.

71. Sharpe, G.J. Linear stability of idealized detonations. *Proc. R. Soc. Lond.* A **1997**, 453, 2603–2625.

72. Sharpe, G.J. Transverse waves in numerical simulations of cellular detonations. *J. Fluid Mech.* **2001**, 447, 31–51.

73. Sharpe, G.J., Falle, S.A.E.G. Numerical simulations of pulsating detonations: I. Non-linear stability of steady detonations. *Combust. Theory. Model.* **2000**, 4, 557–574.

74. Shepherd, J.E. Detonation in gases. *Proc. Combust. Inst.* **2009**, 32(1), 83–98.

75. Short, M., Stewart, D.S. Cellular detonation stability. Part 1. A normal-mode linear analysis. *J. Fluid Mech.* **1998**, 368 (10), 229–262.

76. Smirnov, N.N., Betelin, V.B., Nikitin, V.F., Stamov, L.I., Altoukhov, D.I. Accumulation of errors in numerical simulations of chemically reacting gas dynamics. *Acta Astronaut.* **2015**, 117, 338–355.

77. Smirnov, N.N., Betelin, V.B., Shagaliev, R.M., Nikitin, V.F., Belyakov, I.M., Deryuguin, Yu.N., Aksenov, S.V., Korchazhkin, D.A. Hydrogen fuel rocket engines simulation using LOGOS code. *Int. J. Hydrogen Energy* **2014**, 39, 10748–10756.

78. Strehlow, R.A. *Fundamentals of Combustion*. International Textbook Co., Scranton, PA, **1967**.

79. Strehlow, R.A. The nature of transverse waves in detonations. *Astro. Acta.* **1969**, 5, 539–548.

80. Strehlow, R.A., Liangminas, R., Watson, R.H., Eyman, J.R. Transverse wave structure in detonations. *Proc. Symp. (Int.) on Combust.* **1967**, 11, 683–692.

81. Taki, S., Fujiwara, T. Numerical analysis of two-dimensional non-steady detonations. *AIAA J*. **1978**, 16, 73–77.

82. Tang Yuk, K.C., Mi, X.C., Lee, J.H.S., Ng, H.D. Transmission of a detonation across a density interface. *Shock Waves* **2018**, 28, 967–979.

83. Taylor, B., Kessler, D., Gamezo, V., Oran, E.S. Numerical simulations of hydrogen detonations with detailed chemical kinetics. *Proc. Combust. Inst.* **2013**, 34, 2009–2016.

84. Teng, H.H., Jiang, Z.L. On the transition pattern of the oblique detonation structure. *J. Fluid Mech.* **2012**, 713, 659–669.

85. Teng, H.H., Jiang, Z.L., Ng, H.D. Numerical study on unstable surfaces of oblique detonations. *J. Fluid mech.* **2014**, 744, 111–128.

86. Teng, H.H., Morgan, G.H., Kiyanda, C.B., Nikiforakis, N., Ng, H.D. GPU-based simulation of the two-dimensional unstable structure of gaseous oblique detonations. *AIP Conf. Proc.* **2015**, 1648, 030027.

87. Teng, H.H., Ng, H.D., Li, K., Luo, C.T., Jiang, Z.L. Evolution of cellular structure on oblique detonation surfaces. *Combust. Flame* **2015**, 162, 470–477.

88. Teng, H.H., Zhang, Y.N., Jiang, Z.L. Numerical investigation on the induction zone structure of the oblique detonation waves. *Computers & Fluids* **2014**, 94, 127–131.

89. Toro, E. F. *Riemann Solvers and Numerical Methods for Fluid Dynamics* (3rd ed.). Springer, Berlin, **2006**.

90. Toro, E.F., Billett, S.J. Centred TVD schemes for hyperbolic conservation laws. *IMA J. Numerical Analysis* **2000**, 20(1), 47–79.

91. Toro, E.F., Spruce, M., Speares, W. Restoration of the contact surface in the HLL-Riemann solver. *Shock waves* **1994**, 4(1), 25–34.

92. Toro E.F. A weighted average flux method for hyperbolic conservation laws. *Proc. R. Soc. Lond. A*. **1989**, 423

93. Tsuboi, N., S. Katoh, Hayashi, A.K. Three-dimensional numerical simulation for hydrogen/air detonation: Rectangular and diagonal structures. *Proc. Combust. Inst.* **2002**, 29, 2783–2788.

94. Urzay, J. Supersonic combustion in air-breathing propulsion systems for hypersonic flights. *Annu. Rev. Fluid Mech.* **2018**, 50, 593–627.

95. Vanka S.P. 2012 Freeman Scholar Lecture: Computational Fluid Dynamics on Graphics Processing Units. *ASME. J. Fluids Eng*. **2013**, 135 (6), 061401.

96. Van Albada, G.D., van Leer, B., Roberts, W.W. A comparative study of computational methods in cosmic gas dynamics. *Astron. Astrophys.* **1982**, 108(1), 76–84.

97. Van Leer, B. On the relation between the upwind-differencing schemes of Godunov, Enguist-Osher and Roe. *SIAM J. Sci. Comput.* **1984**, 5(1), 1–20.

98. Verreault, J., Higgins, A.J. Initiation of Detonation by. Conical Projectiles. *Proc. Combust. Inst.* **2011**, 33 (2), 2311–2318.

99. Verreault, J., Higgins, A.J., Stowe, R.A. Formation of transverse waves in oblique detonations. *Proc. Combust. Inst.* **2013**, 34, 1913–1920.

100. Viguier, C., Figueira da Silva, L.F., Desbordes, D., Deshaies, B. Onset of oblique detonation waves: Comparison between experimental and numerical results for hydrogen-air mixtures. *Symp. (Int.) Combust.* **1996**, 26, 3023–3031.

101. Vlasenko, V.V., Sabel'nikov, V.A. Numerical simulation of inviscid flows with hydrogen combustion behind shock waves and in detonation waves. *Combust. Explos. Shock Waves* **1995**, 31, 376–389.

102. von Neumann, J. *Theory of Detonation Wave. John von Neumann, Collected Works*. Vol. 6. Macmillan, New York, **1942**.

103. Wang, T., Zhang, Y., Teng, H., Jiang, Z., Ng, H.D., Numerical study of oblique detonation wave initiation in a stoichiometric hydrogen-air mixture. *Phys. Fluids* **2015**, 27, 96–101.

104. White, D.R. Turbulent structure of gaseous detonation. *Phys. Fluids* **1961**, 4, 465–480.

105. Williams, D.N., Bauwens, L., Oran, E.S. Detailed structure and propagation of three-dimensional detonations. *Proc. Combust. Inst.* **1997**, 26, 2991–2998.

106. Wolanski, P. Detonation propulsion. *Proc. Combust. Inst.* **2013**, 34, 125–158.

107. Yang, P., Teng, H., Ng, H.D., Jiang, Z.L. A numerical study on the instability of oblique detonation waves with a two-step induction–reaction kinetic model, *Proc. Combust. Inst.* **2018**, 37 (3), 3537–3544.

108. Zel'dovich, Y.B. On the theory of the propagation of detonation in gaseous systems. *Zh. Eksp. Teor. Fiz.* **1940**, 10, 542–568.

109. Zhang, Y., Yang, P., Teng, H., Ng, H.D. Wen, C. Transition between different initiation structures of wedge-induced oblique detonations. *AIAA J.* **2018**, 56 (10), 4016–4023.

110. Zhang, Y., Zhou, L., Gong, J., Deng, X., Ng, H.D., Teng, H.H. Effects of activation energy on the instability of oblique detonation surfaces with a one-step chemistry model. *Phys. Fluids* **2018**, 30, 106110.

111. Ziegler, J.L., Deiterding, R., Shepherd, J.E., Pullin, D.I. An adaptive high-order hybrid scheme for compressive, viscous flows with detailed chemistry. *J. Comput. Phys.* **2011**, 230, 7598–7630.